NEW CONSTRAINTS ON THE EVOLUTION OF THE STELLAR-TO-DARK MATTER CONNECTION: A COMBINED ANALYSIS OF GALAXY–GALAXY LENSING, CLUSTERING, AND STELLAR MASS FUNCTIONS FROM $z = 0.2$ TO $z = 1^{*}$

ALEXIE LEAUTHAUD[1,2,3], JEREMY TINKER[4], KEVIN BUNDY[5], PETER S. BEHROOZI[6], RICHARD MASSEY[7], JASON RHODES[8,9], MATTHEW R. GEORGE[5], JEAN-PAUL KNEIB[10], ANDREW BENSON[8], RISA H. WECHSLER[6], MICHAEL T. BUSHA[6,11], PETER CAPAK[12], MARINA CORTÊS[2], OLIVIER ILBERT[10], ANTON M. KOEKEMOER[13], OLIVER LE FÈVRE[10], SIMON LILLY[14], HENRY J. MCCRACKEN[15], MARA SALVATO[16], TIM SCHRABBACK[6,17], NICK SCOVILLE[8], TRISTAN SMITH[3], AND JAMES E. TAYLOR[18]

[1] Institute for the Physics and Mathematics of the Universe, The University of Tokyo, Chiba 277-8582, Japan
[2] Lawrence Berkeley National Lab, 1 Cyclotron Road, Berkeley, CA 94720, USA; asleauthaud@lbl.gov
[3] Berkeley Center for Cosmological Physics, University of California, Berkeley, CA 94720, USA
[4] Center for Cosmology and Particle Physics, Department of Physics, New York University, NY, USA
[5] Department of Astronomy, University of California, Berkeley, CA 94720, USA
[6] Kavli Institute for Particle Astrophysics and Cosmology, Physics Department, Stanford University, and SLAC National Accelerator Laboratory, Stanford, CA 94305, USA
[7] Institute for Astronomy, Blackford Hill, Edinburgh EH9 3HJ, UK
[8] California Institute of Technology, MC 350-17, 1200 East California Boulevard, Pasadena, CA 91125, USA
[9] Jet Propulsion Laboratory, California Institute of Technology, Pasadena, CA 91109, USA
[10] LAM, CNRS-UNiv Aix-Marseille, 38 rue F. Joliot-Curis, 13013 Marseille, France
[11] Institute for Theoretical Physics, Department of Physics, University of Zurich, CH-8057, Switzerland
[12] Spitzer Science Center, 314-6 Caltech, 1201 E. California Blvd. Pasadena, CA 91125, USA
[13] Space Telescope Science Institute, 3700 San Martin Drive, Baltimore, MD 21218, USA
[14] Institute of Astronomy, Department of Physics, ETH Zurich, CH-8093, Switzerland
[15] Institut d'Astrophysique de Paris, UMR 7095, 98 bis Boulevard Arago, 75014 Paris, France
[16] SUPA, Institute for Astronomy, The University of Edinburgh, Royal Observatory, Edinburgh EH9 3HJ, UK
[17] Leiden Observatory, Leiden University, Niels Bohrweg 2, NL-2333 CA Leiden, The Netherlands
[18] Department of Physics and Astronomy, University of Waterloo, 200 University Avenue West, Waterloo, ON N2L 3G1, Canada

ABSTRACT

Using data from the COSMOS survey, we perform the first joint analysis of galaxy–galaxy weak lensing, galaxy spatial clustering, and galaxy number densities. Carefully accounting for sample variance and for scatter between stellar and halo mass, we model all three observables simultaneously using a novel and self-consistent theoretical framework. Our results provide strong constraints on the shape and redshift evolution of the stellar-to-halo mass relation (SHMR) from $z = 0.2$ to $z = 1$. At low stellar mass, we find that halo mass scales as $M_h \propto M_*^{0.46}$ and that this scaling does not evolve significantly with redshift from $z = 0.2$ to $z = 1$. The slope of the SHMR rises sharply at $M_* > 5 \times 10^{10} M_\odot$ and as a consequence, the stellar mass of a central galaxy becomes a poor tracer of its parent halo mass. We show that the dark-to-stellar ratio, M_h/M_*, varies from low to high masses, reaching a minimum of $M_h/M_* \sim 27$ at $M_* = 4.5 \times 10^{10} M_\odot$ and $M_h = 1.2 \times 10^{12} M_\odot$. This minimum is important for models of galaxy formation because it marks the mass at which the accumulated stellar growth of the central galaxy has been the most efficient. We describe the SHMR at this minimum in terms of the "pivot stellar mass," M_*^{piv}, the "pivot halo mass," M_h^{piv}, and the "pivot ratio," $(M_h/M_*)^{\mathrm{piv}}$. Thanks to a homogeneous analysis of a single data set spanning a large redshift range, we report the first detection of mass downsizing trends for both M_h^{piv} and M_*^{piv}. The pivot stellar mass decreases from $M_*^{\mathrm{piv}} = 5.75 \pm 0.13 \times 10^{10} M_\odot$ at $z = 0.88$ to $M_*^{\mathrm{piv}} = 3.55 \pm 0.17 \times 10^{10} M_\odot$ at $z = 0.37$. Intriguingly, however, the corresponding evolution of M_h^{piv} leaves the pivot ratio constant with redshift at $(M_h/M_*)^{\mathrm{piv}} \sim 27$. We use simple arguments to show how this result raises the possibility that star formation quenching may ultimately depend on M_h/M_* and not simply on M_h, as is commonly assumed. We show that simple models with such a dependence naturally lead to downsizing in the sites of star formation. Finally, we discuss the implications of our results in the context of popular quenching models, including disk instabilities and active galactic nucleus feedback.

Key words: dark matter – galaxies: evolution – galaxies: formation – galaxies: luminosity function, mass function – galaxies: stellar content – gravitational lensing: weak

Online-only material: color figures

---

1. INTRODUCTION

A fundamental goal in observational cosmology is to understand the link between the luminous properties of galaxies and the dark matter halos in which they reside. From an astrophysical perspective, measurements of the relationship between dark matter halo mass (M_h) and galaxy observables such as luminosity or stellar mass (M_*) are critical for understanding how galaxy properties and their evolution with time are shaped by the halos that host them. Growing evidence suggests that halos accumulate stellar mass with an efficiency $\eta(M_h, z) \equiv (M_*/M_h) \times (\Omega_M/\Omega_b)$ that depends strongly on halo mass, peaking at $M_h \sim 10^{12} M_\odot$ and declining toward lower and higher masses at $z \sim 0$ (e.g., Mandelbaum et al. 2006b; Conroy & Wechsler 2009; Moster et al. 2010; Behroozi et al. 2010; Guo et al. 2010; More et al. 2010). The stellar mass content is determined by the past merging of smaller sub-components but also by processes that regulate the conversion of gas into stars, including the rate at which fresh material is supplied to the halo, feedback mechanisms from supernovae, galactic winds, and active galactic nuclei (AGNs), and environmental effects such as ram pressure stripping, just to name a few. The global relationship between halo mass and average stellar content—the stellar-to-halo mass relation (SHMR)—probes the integrated outcome of these processes and, as such, provides clues to their physical nature and constrains both semi-analytic models (e.g., Bower et al. 2006; Croton et al. 2006; Somerville et al. 2008; Zehavi et al. 2011a) and hydrodynamical simulations (Kereš et al. 2005, 2009; Crain et al. 2009; Brooks et al. 2009; Gabor et al. 2011; Agertz et al. 2011) that aim to disentangle the relative contributions of such mechanisms.

From a cosmological perspective, the SHMR is vital for determining how galaxies trace dark matter. A complete picture of the manner in which galaxies populate dark matter halos enhances the reconstruction of the dark matter power spectrum from redshift surveys (Sánchez & Cole 2008; Yoo et al. 2009) and leads to improved constraints on cosmological parameters (Yoo et al. 2006; Zheng & Weinberg 2007; Cacciato et al. 2009).

There are currently only two observational techniques capable of *directly* probing the dark matter halos of galaxies out to large radii (above 50 kpc): galaxy–galaxy lensing (e.g., Brainerd et al. 1996; McKay et al. 2001; Hoekstra et al. 2004; Sheldon et al. 2004, 2009; Mandelbaum et al. 2006a, 2006b; Heymans et al. 2006a; Johnston et al. 2007; Leauthaud et al. 2010) and the kinematics of satellite galaxies (McKay et al. 2002; Prada et al. 2003; Brainerd & Specian 2003; van den Bosch et al. 2004; Conroy et al. 2007; Becker et al. 2007; Norberg et al. 2008; More et al. 2009, 2010). The galaxy–galaxy lensing technique (hereafter "g–g lensing") uses weak gravitational lensing to probe the gravitational potential around foreground ("lens") galaxies. The kinematic method uses satellite galaxies as test particles that trace the local velocity field (and hence the local gravitational potential).

Another popular albeit more indirect method to infer the galaxy–dark matter connection is to measure the statistics of galaxy clustering. The results are commonly interpreted using the Halo Occupation Distribution (HOD) model which describes the probability distribution $P(N|M_h)$ that a halo of mass M_h is host to N galaxies above some threshold in luminosity or stellar mass (e.g., Seljak 2000; Peacock & Smith 2000; Scoccimarro et al. 2001; Berlind & Weinberg 2002; Bullock et al. 2002; Zehavi et al. 2002, 2005, 2011b; Zheng et al. 2005, 2007; Tinker

et al. 2007; Skibba & Sheth 2009; Brown et al. 2008; Wake et al. 2011; Foucaud et al. 2010; White et al. 2011). Variations on the HOD approach include the conditional luminosity function $\Phi(L|M_h)dL$ which specifies the average number of galaxies of luminosity $L \pm dL/2$ that reside in a halo of mass M_h (e.g., Yang et al. 2003; van den Bosch et al. 2003, 2007; Vale & Ostriker 2004, 2008; Cooray 2006) and the conditional stellar mass function (SMF) $\Phi(M_*|M_h)dM_*$ which yields the average number of galaxies with stellar masses in the range $M_* \pm dM_*/2$ as a function of host halo mass M_h (e.g., Yang et al. 2009; Moster et al. 2010; Behroozi et al. 2010).

Finally, constraints on the SHMR have also been derived from the so-called abundance matching technique, which assumes that there is a monotonic correspondence between halo mass (or circular velocity) and galaxy stellar mass (or luminosity) (e.g., Kravtsov et al. 2004; Vale & Ostriker 2004, 2006; Tasitsiomi et al. 2004; Conroy & Wechsler 2009; Drory et al. 2009; Moster et al. 2010; Behroozi et al. 2010; Guo et al. 2010).

While individual applications of the techniques described above have provided important insight, in Leauthaud et al. (2011b, hereafter Paper I) we take a further step by *combining* separate probes into a self-consistent theoretical framework. Specifically, our method combines measurements of g–g lensing, galaxy clustering, and the galaxy SMF. Beginning with the standard HOD formalism, we make several modifications that enable us to (1) extract the parameters that determine the SHMR and to (2) simultaneously fit data from multiple probes while allowing for independent binning schemes for each probe. The goal of the current paper is to apply the methodology developed in Paper I to observations from the COSMOS survey from $z = 0.2$ to $z = 1.0$. This enables confident measurements of the shape of the SHMR and its evolution with time, with important implications for models of galaxy formation. In Paper III (Leauthaud et al. 2011b), we will use the HOD constraints from this paper to probe the total stellar content of dark matter halos.

While stellar mass estimates are a key galaxy observable in this work, it is important to highlight the uncertainties and sometimes unknown systematic biases that affect them and, if not treated carefully, can muddle attempts to compare results from disparate surveys (see discussion in Behroozi et al. 2010). One of the advantages of the COSMOS data set is that evolutionary trends can be studied within the sample using self-consistent stellar mass estimates, making our conclusions more robust.

The layout of this paper is as follows. The data are described in Section 2 followed by the presentation of the g–g lensing, clustering, and SMF measurements in Section 3. In the interest of brevity, we only give a short and necessarily incomplete review of the theoretical background in Section 4. We strongly encourage the reader to refer to Paper I for a complete description of the theoretical foundations for this work. Our main results are presented in Section 5. Finally, we discuss the results and draw up our conclusions in Sections 6 and 7.

We assume a WMAP5 ΛCDM cosmology with $\Omega_m = 0.258$, $\Omega_\Lambda = 0.742$, $\Omega_b h^2 = 0.02273$, $n_s = 0.963$, $\sigma_8 = 0.796$, $H_0 = 72$ km s^{-1} Mpc^{-1} (Hinshaw et al. 2009). All distances are expressed in physical Mpc units. The letter M_h denotes halo mass in general whereas M_{200b} is explicitly defined as $M_{200b} \equiv M(< r_{200b}) = 200\bar{\rho}\frac{4}{3}\pi r_{200b}^3$, where r_{200b} is the radius at which the mean interior density is equal to 200 times the mean matter density ($\bar{\rho}$). Stellar mass is denoted M_* and has been derived using a Chabrier initial mass function (IMF).

Stellar mass scales as $1/H_0^2$. Halo mass scales as $1/H_0$. All magnitudes are given on the AB system.

2. DESCRIPTION OF DATA

The COSMOS survey (Scoville et al. 2007) brings together a broad array of panchromatic observations with imaging data from X-ray to radio wavelengths and a large spectroscopic follow-up program (zCOSMOS) with the Very Large Telescope (VLT; Lilly et al. 2007). In particular, the COSMOS program has imaged the largest contiguous area (1.64 deg^2) to date with the *Hubble Space Telescope*(*HST*) using the Advanced Camera for Surveys (ACS) Wide Field Channel (WFC; Koekemoer et al. 2007).

2.1. The ACS Lensing Catalog

The general methodology for the construction of the COS-MOS ACS weak lensing catalog and our shape measurement procedure are presented in Leauthaud et al. (2007) and Rhodes et al. (2007). In this section, we present several updates to the pipeline that we have implemented since those publications. In Leauthaud et al. (2007), we used a parametric correction for the effects of charge transfer inefficiency (CTI) on galaxy shape measurements. Instead, in this paper, we use a physically motivated CTI correction scheme that operates on the raw data and returns electrons to pixels from which they were unintentionally dragged out during readout. This correction scheme has been shown by Massey et al. (2010) to reduce the CTI trails by a factor of ∼10 everywhere in the CCD and at all flux levels.

Following CTI correction in the raw images, image registration, geometric distortion, sky-subtraction, cosmic ray rejection, and the final combination of the dithered images are performed by the MultiDrizzle algorithm (Koekemoer et al. 2002). As described in Rhodes et al. (2007), a finer pixel scale of $0.''03\,\mathrm{pixel}^{-1}$ was used for the final co-added images. The lensing source catalog is constructed from 575 ACS/WFC tiles. Defects and diffraction spikes are carefully removed, leaving a total of 1.2×10^6 objects to a limiting magnitude of $I_{F814W} = 26.5$.

The next step is to measure the shapes of galaxies and to correct them for the distortion induced by the time varying ACS point-spread function (PSF; see Rhodes et al. 2007). We continue to use a PSF model based on physical parameters rather than arbitrary principal components. In Leauthaud et al. (2007), we modeled the PSF as a multivariate polynomial in x, y, and focus. We now fit the PSF as a function of x, y, focus, and velocity aberration of the pointing (recorded in CALACS headers as "VAFACTOR"). Schrabback et al. (2010) found that VAFACTOR partially correlates with the higher-order PSF variations, motivating our use of this quantity. In the g–g lensing analysis presented here, the weak lensing shear is azimuthally averaged. Thus, any effects of PSF anisotropy cancel to leading order. Therefore, our science analysis is insensitive to subtle differences in the PSF modeling. We confirmed this by repeating our analysis with the independently obtained weak lensing catalog by Schrabback et al. (2010), which yields fully consistent results.

Finally, simulated images are used to derive the shear susceptibility factors that are necessary in order to transform shape measurements into unbiased shear estimators (Leauthaud et al. 2007). Representing a number density of 66 galaxies per arcminute^2, the final COSMOS weak lensing catalog contains 3.9×10^5 galaxies with accurate shape measurements.

2.2. Photometric and Spectroscopic Redshifts

We use two updated versions (v1.8 dated from 2010 July 13 and v1.7 dated from 2009 August 1) of the photometric redshifts (hereafter photo-z's) presented in Ilbert et al. (2009) which have been computed with over 30 bands of multi-wavelength data. In particular, deep K_s, J, and u^* band data allow for a good photo-z estimate at $z > 1$ via the 4000 Å break which is increasingly shifted into the near-infrared (IR). Further details regarding the data and the photometry can be found in Capak et al. (2007).

The photo-z catalog v1.8 has improved redshifts at $z > 1$ compared to v1.7. At $z < 1$, the difference between the two catalogs is minor. We use catalog v1.8 for g–g lensing measurements and v1.7 for the SMF and galaxy clustering. Interchanging the two catalogs does not affect our results.

Photo-z's were estimated using a χ^2 template fitting method (Le Phare; Ilbert et al. 2009) and calibrated with large spectroscopic samples from VLT-VIMOS (Lilly et al. 2007) and Keck-DEIMOS. The dispersion in the photo-z's as measured by comparing to the spectroscopic redshifts is $\sigma_{\Delta z/(1+z_{spec})} = 0.007$ at $i_{AB}^+ < 22.5$, where $\Delta z = z_{spec} - z_{phot}$. The deep IR and IRAC (Infrared Array Camera on the *Spitzer Space Telescope*) data enable the photo-z's to be calculated even at fainter magnitudes with a reasonable accuracy of $\sigma_{\Delta z/(1+z_{spec})} = 0.06$ at $i_{AB}^+ \sim 24$ mag.

Figure 1 compares the spectroscopic and photometric redshifts of 8812 galaxies that belong to both the lensing source catalog and the zCOSMOS "bright" or "faint" programs. This figure also illustrates the sensitivity of g–g lensing signals to photometric redshift errors. As can be seen from Figure 1, g–g lensing signals are increasingly insensitive to photometric redshift errors for source galaxies at higher redshifts.

2.3. Stellar Mass Estimates

Stellar masses are estimated using the Bayesian code described in Bundy et al. (2006) assuming a Chabrier IMF. Briefly, an observed galaxy's spectral energy distribution (SED) and redshift is referenced to a grid of models constructed using the Bruzual & Charlot (2003) synthesis code. The grid includes models that vary in age, star formation history, dust content, and metallicity. The assumed dust model is Charlot & Fall (2000). At each grid point, the probability that the observed SED fits the model is calculated, and the corresponding stellar mass to K-band luminosity ratio and stellar mass is stored. By marginalizing over all parameters in the grid, the stellar mass probability distribution is obtained. The median of this distribution is taken as the stellar mass estimate, and the width encodes the uncertainty due to degeneracies and uncertainties in the model parameter space (also described as "model error" in Section 4.2). The final uncertainty on the stellar mass also includes the K-band photometry uncertainty as well as the expected error on the luminosity distance that results from the photo-z uncertainty. The typical final uncertainty is 0.1–0.2 dex (also see Section 4.2 and Figure 4). Systematic uncertainties also come from the choice of stellar population templates used to fit the data as well as the assumption of a universal IMF. To first order these will cause global offsets in the mass estimates that will not affect comparisons *within* our sample but may impact comparisons to work by other authors. Since the primary goal of this paper is to study the redshift evolution of the SHMR derived from COSMOS data alone, we do not include these systematic uncertainties in our analysis and refer to Conroy et al. (2009) and Behroozi et al.
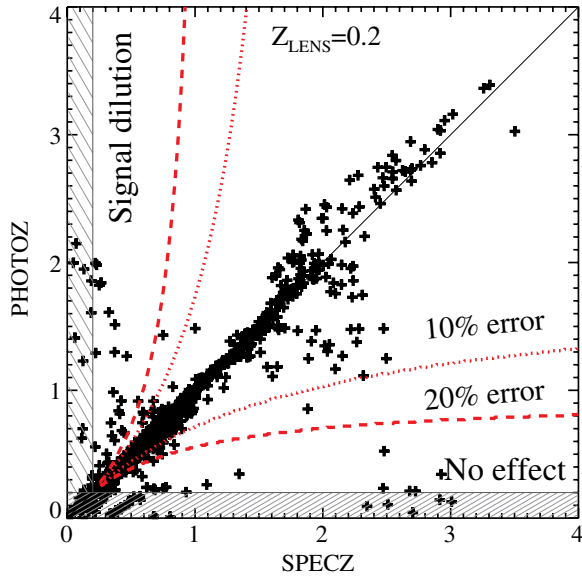
Figure 1. Effects of photometric redshift errors on galaxy–galaxy lensing signals. This figure illustrates the quality of the photometric redshifts for source galaxies in this paper by comparing them to a combined sample of 8812 spectroscopic redshifts from the zCOSMOS "bright" and "faint" programs for which we have applied the same selection as for source galaxies. We emphasize that since the spectroscopic sample does not go as faint as our source catalog, this figure is necessarily an underestimate of the true redshift errors for the source catalog—a complete sample of faint galaxies with spectroscopic redshift would be necessary in order to fully test the photometric redshifts. There are three ways in which photometric redshift errors can impact g–g lensing signals. First, any type of photometric error such that $z_{phot} < z_{lens}$ will have no effect on the signal because such objects are not included in the background selection (bottom hashed region). Second, photometric errors such that $z_{phot} > z_{lens}$ and $z_{spec} < z_{lens}$ will lead to a signal dilution (left hashed region). Finally, photometric errors such that $z_{phot} > z_{lens}$ and $z_{spec} > z_{lens}$ but $z_{phot} \neq z_{spec}$ will lead to a bias in $\Delta\Sigma$ (the surface mass density contrast) because Σ_{crit} will be misestimated when transforming γ (gravitational shear) into $\Delta\Sigma$. The dotted and dashed lines indicate where photo-z errors lead to a 10% and a 20% error on $\Delta\Sigma$ for a lens located at $z = 0.2$. As can be seen, g–g lensing signals are increasingly insensitive to photometric redshift errors for source galaxies at higher redshifts.

(A color version of this figure is available in the online journal.)

Figure 2. Distribution of COSMOS galaxies as a function of redshift and stellar mass. The completeness limit for passive galaxies is shown by the red dashed line and for star-forming galaxies by the blue dotted line (see Section 2.3 for the derivation of the completeness limits). The green hashed region approximately shows the cross-over mass above which the number of red galaxies becomes larger than the number of blue galaxies. The vertical solid dark blue lines delineate the three redshift bins z_1, z_2, and z_3 while the horizontal solid dark blue lines show the binning scheme for the g–g lensing measurements.

(A color version of this figure is available in the online journal.)

(2010) for a broad discussion of systematic errors in stellar mass estimates.

Following the approach in Bundy et al. (2010), we obtained PSF-matched $3''.0$ diameter aperture photometry from the ground-based COSMOS catalogs (filters u^*, B_J, V_J, g^+, r^+, i^+, z^+, K_s) described in Capak et al. (2007), Ilbert et al. (2009), and McCracken et al. (2010), after applying the photometric zero-point offsets tabulated in Capak et al. (2007). The depth in all bands reaches at least 25th magnitude (AB) with the K_s-band limited to $K_s < 24$ mag. Unlike Drory et al. (2009), we require K_s-band detections for all galaxies in the sample. We have found that the mass estimates in Bundy et al. (2010) agree with those of Drory et al. (2009) within the expected uncertainties (i.e., <0.2 dex). The mass estimates used in this work are slightly different from those in Bundy et al. (2010) in that they are based on updated redshift information (v1.7 of the photo-z catalog and the latest available spectroscopic redshifts as compiled by the COSMOS team) and use a slightly different cosmology ($H_0 = 72$ km s^{-1} Mpc^{-1} instead of $H_0 = 70$ km s^{-1} Mpc^{-1}).

The bins in our analysis are defined by using two estimates of the mass completeness of the sample, as determined by the magnitude limits $K_s < 24$ mag and $I_{814W} < 25$ mag. The first estimate is more conservative and comes from estimating
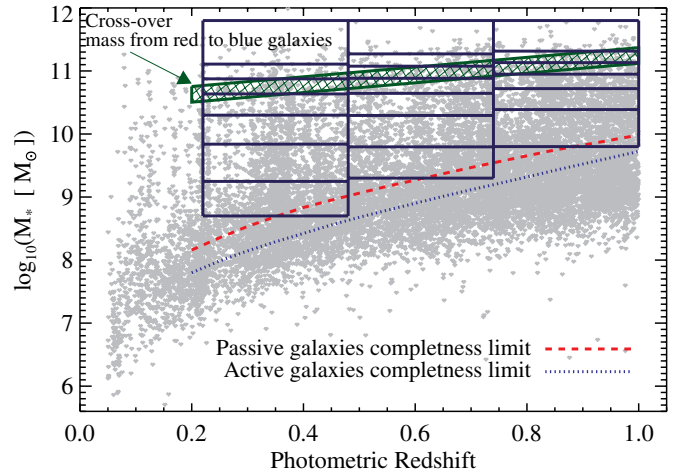
the observed magnitude of a maximal M_*/L stellar population model with solar metallicity, no dust, and a $\tau = 0.5$ Gyr burst of star formation that occurred at $z_{form} = 5$. As a function of redshift, the stellar mass of such a population at the point where its observed K_s- and I_{814W}-band flux falls below the magnitude limits defines the mass completeness and roughly matches the 80% completeness limits determined when deeper samples are available (Bundy et al. 2006). This redshift-dependent limit is plotted as the dashed line in Figure 2. In practice, low-mass galaxies exhibit more star formation and therefore have lower M_*/L ratios than the passive template described above so we also define a second, more liberal mass limit (i.e., lower) that corresponds to a star-forming population. This is plotted as the dotted line. The majority of the sample bins lie above the more conservative limit, but the lowest mass bins are allowed to reach the star-forming mass limit under the assumption that passive stellar populations (potentially missed) at such low masses are extremely rare.

3. MEASUREMENTS

3.1. Sample Selection

We use two COSMOS galaxy catalogs: the Subaru (photo-z) catalog and the ACS (lensing) catalog. The ACS catalog corresponds to the COSMOS area that has been imaged with *HST* and covers a slightly smaller area than the Subaru catalog. The ACS coverage of COSMOS is 1.64 deg^2 and the Subaru coverage of COSMOS is 2.3 deg^2. The ACS catalog is used for our g–g lensing measurements and for the SMFs. The Subaru catalog is used to calculate the galaxy clustering.

Galaxies are selected with $K_s < 24$ mag to ensure that stellar masses can be computed for all galaxies in the sample. Note that for the g–g lensing analysis, these cuts only apply to the foreground lens sample. In addition to these cuts, we also reject galaxies that are in masked areas where the photometry is deemed unreliable. For this, we use the union of four masks in the B_J, V_J, i^+, and z^+ ("COSMOS.B.mask," "COSMOS.V.mask," "COSMOS.ip.mask," and "COSMOS.zp.mask").

Table 1
Characteristics of Three Redshift Bins

z_{min}	z_{max}	z Median	ACS Volume (10^6 Mpc^3)	Subaru Volume (10^6 Mpc^3)	Min M_*	N Galaxies ACS[a]	N Galaxies Subaru[a]
0.22	0.48	0.37	0.88	1.24	$10^{8.7}\ M_\odot$	14956	20426
0.48	0.74	0.66	2.03	2.84	$10^{9.3}\ M_\odot$	15103	20068
0.74	1.0	0.88	3.13	4.39	$10^{9.8}\ M_\odot$	14387	18853

Note. [a] Numbers are quoted after stars have been removed, the selection $K_s < 24$ as well as the lower limit stellar mass limit has been applied, and objects in masked areas have been removed from the catalog.

Table 2
Thresholds for the Angular Correlation Function

	w bin1	w bin2	w bin3	w bin4	w bin5	w bin6
Minimum $\log_{10}(M_*)$, $z_1 = [0.22, 0.48]$	11.1	10.8	10.3	9.8	9.3	8.8
Minimum $\log_{10}(M_*)$, $z_2 = [0.48, 0.74]$	11.1	10.8	10.3	9.8	9.3	None
Minimum $\log_{10}(M_*)$, $z_3 = [0.74, 1.0]$	11.1	10.8	10.3	9.8	None	None

For the ACS sample, star–galaxy separation is performed using the morphological classifier described in Leauthaud et al. (2007). For the Subaru sample, we reject stars by imposing the condition that $\chi^2_{gal} - \chi^2_{star} > 0.5$ where χ^2_{gal} represents the chi-square value of the best-fitting galaxy SED template and χ^2_{star} represents the chi-square value of the best-fitting stellar SED template. In conjunction with the K_s cut, this stellar selection agrees with our ACS-based morphological classification at the 97% level. According to our ACS morphological classifier: 2% of the objects (or 5095 objects in the ACS area) in the final Subaru catalog are classified as stars and 0.1% of galaxies are misclassified as stars (or 246 objects in the ACS area) so the stellar sample reliability is 0.048.

We compute the g–g lensing, galaxy clustering, and stellar mass in three redshift intervals: $z_1 = [0.22, 0.48]$, $z_2 = [0.48, 0.74]$, and $z_3 = [0.74, 1]$. For each redshift bin, we define a lower limit on the stellar mass to ensure that all samples are complete in terms of stellar mass. These cuts correspond to $M_* > 10^{8.7}\ M_\odot$ for z_1, $M_* > 10^{9.3}\ M_\odot$ for z_2, and $M_* > 10^{9.8}\ M_\odot$ for z_3 (see Table 1) and are defined by the stellar mass completeness limit at the far edge of the redshift bin (see Figure 2). All galaxy samples used in this paper are complete.

3.2. Stellar Mass Functions

The SMFs are calculated using the ACS catalog. As in Bundy et al. (2010), we compute mass functions using the V_{max} technique (Schmidt 1968). We weight galaxies by the maximum volume in which they would be detected within the K_s-band and I_{814W}-band limits in a given redshift interval. For each host galaxy i in the redshift interval j, the value of V^i_{max} is given by the minimum redshift at which the galaxy would drop out of the sample,

$$V^i_{max} = \int_{z_{low}}^{z_{high}} d\Omega \frac{dV}{dz} dz, \qquad (1)$$

where $d\Omega$ is the solid angle subtended by the survey area and dV/dz is the comoving volume element. The redshift limits are given as

$$z_{high} = \min\left(z^j_{max}, z^j_{K_{lim}}, z^j_{I_{lim}}\right), \qquad (2)$$

$$z_{low} = z^j_{min}, \qquad (3)$$

where the redshift interval, j, is defined by $[z^j_{min}, z^j_{max}]$ and $z^j_{K_{lim}}$ and $z^j_{I_{lim}}$ refer to the redshift (see Table 1 for the redshift limits) at which the galaxy would still be detected below the K_s- and I_{814W}-band limits. We use the best-fit SED template as determined by the stellar mass estimator to calculate these values, thereby accounting for the k-corrections necessary to compute V_{max} values (no evolutionary correction is applied).

3.3. Galaxy Autocorrelation Function

The galaxy clustering samples are defined by a series of stellar mass thresholds rather than bins. For galaxy clustering, threshold samples are the most straightforward to model in the HOD context. At small scales, the signal-to-noise ratio (S/N) in galaxy clustering is due mostly to Poisson noise and at large scales it is subject to sample ("cosmic") variance. The optimal binning scheme for clustering can be different than that for g–g lensing. For example, massive galaxies produce the strongest shear signals, thus a relatively small sample is required to produce a robust measurement relative to a simple pair-counting statistic like the two-point correlation function whereas the inverse would be true for low-mass galaxies. The threshold samples we employ for clustering measurements are listed in Table 2. Except at the high-mass end where galaxies become scarce, the binning scheme employed for the clustering is a constant 0.5 dex in $\log_{10}(M_*)$.

Since we do not need galaxy shape information to measure the angular correlation function $w(\theta)$, we are not restricted to the ACS coverage of the COSMOS field. We therefore use the COSMOS Subaru catalog to calculate $w(\theta)$. For each threshold sample we measure $w(\theta)$ using the well-known Landy & Szalay (1993) estimator of

$$w(\theta) = \frac{DD - 2DR + RR}{RR}, \qquad (4)$$

where DD are the number of data–data pairs in a given bin of angle θ, RR are the number of random–random pairs, and DR are the number of data–random pairs. Data and random pairs are normalized by the total number of galaxies and random points, respectively. In all measurements we use 10^5 random points. The distribution of the random points is taken from a combination of four COSMOS masks (B_J, V_J, i^+, and z^+), thus mimicking the angular completeness and geometry of the survey.

Because the volumes probed in each sample are small, our clustering measurements are subject to the effect of the integral

constraint (IC; Groth & Peebles 1977). Due to spatial fluctuations in the number density of galaxies, the mean correlation function measured from an ensemble of samples will be smaller than the correlation function measured from a single contiguous sample of the same volume as the sum of the ensemble sample. This attenuation of $w(\theta)$ becomes relevant on angular scales significant with respect to the sample size. We estimate the IC correction to our $w(\theta)$ measurements through the use of mock galaxy distributions described in Paper I and Section 4. In practice, we do not modify the measurements for the IC but rather adjust the theoretical models to account for the finite sample size.

Finally, in order to compute $w(\theta)$ from our model, we need to know the normalized redshift distribution of the galaxy sample, $N(z)$ (see Equation (32) in Paper I). For this we use the probability distribution functions of the photometric redshifts to estimate the true $N(z)$ for our photo-z slices. However, the COSMOS photo-z errors are accurate enough such that in tests we find a minimal effect when using a flat top-hat z-bin for $N(z)$.

3.4. Galaxy–Galaxy Lensing: From Galaxy Shapes to $\Delta\Sigma$

In the weak gravitational lensing limit, the observed shape $\varepsilon_{\rm obs}$ of a source galaxy is directly related to the lensing induced shear γ according to

$$\varepsilon_{\rm obs} = \varepsilon_{\rm int} + \gamma, \tag{5}$$

where $\varepsilon_{\rm int}$ is the source galaxy's intrinsic shape that would be observed in the absence of gravitational lensing. In our notation, $\varepsilon_{\rm int}$, $\varepsilon_{\rm obs}$, and γ are spin-2 tensors. The above relationship indicates that galaxies would be ideal tracers of the distortions caused by gravitational lensing if the intrinsic shape $\varepsilon_{\rm int}$ of each source galaxy was known a priori. However, lensing measurements exhibit an intrinsic limitation, encoded in the width of the ellipticity distribution of the galaxy population, denoted here as $\sigma_{\rm int}$, and often referred to as the "intrinsic shape noise." Because the intrinsic shape noise (of order $\sigma_{\rm int} \sim 0.27$; Leauthaud et al. 2007) is significantly larger than γ, shears must be estimated by averaging over a large number of source galaxies.

Throughout this paper, the gravitational shear is noted as γ whereas $\tilde{\gamma}$ represents our estimator of γ. The uncertainty in the shear estimator is a combination of unavoidable intrinsic shape noise, $\sigma_{\rm int} = \sqrt{\langle \varepsilon_{\rm int}^2 \rangle}$, and of shape measurement error, $\sigma_{\rm meas}$:

$$\sigma_{\tilde{\gamma}}^2 = \sigma_{\rm int}^2 + \sigma_{\rm meas}^2. \tag{6}$$

We will refer to $\sigma_{\tilde{\gamma}}$ as "shape noise" whereas $\sigma_{\rm int}$ will be called the "intrinsic shape noise." The former includes shape measurement error and will vary according to each specific data set and shape measurement method. Averaged over the whole COSMOS field, the weak lensing distortions represent a negligible perturbation to Equation (6).

The derivation of our shear estimator is presented in Leauthaud et al. (2007). We employ the RRG method (see Rhodes et al. 2000 for further details) for galaxy shape measurements. Briefly, we form $\tilde{\gamma}$ from the PSF-corrected ellipticity according to

$$\tilde{\gamma} = C \times \frac{\varepsilon_{\rm obs}}{G}, \tag{7}$$

where the shear susceptibility factor,[19] G, is measured from moments of the global distribution of $\varepsilon_{\rm obs}$ and other, higher-

order shape parameters (see Equation (28) in Rhodes et al. 2000). Using a set of simulated images similar to those of Shear TEsting Program (STEP; Heymans et al. 2006b; Massey et al. 2007) but tailored exclusively to this data set, we find that, in order to correctly measure the input shear on COSMOS-like images, the RRG method requires an overall calibration factor of $C = (0.86^{+0.07}_{-0.05})^{-1}$. Shear calibration factors are a generic feature of all shape measurement algorithms. This is because no shear measurement technique is independent of the observing conditions and the underlying galaxy population (Massey et al. 2007; Bernstein 2010; Zhang & Komatsu 2011). Thus, it is a common practice in weak lensing measurements to derive survey-specific calibration factors using simulations designed to mimic both the observing conditions and the surveyed galaxy population.

The shear signal induced by a given foreground mass distribution on a background source galaxy will depend on the transverse proper distance between the lens and the source and on the redshift configuration of the lens–source system. A lens with a projected surface mass density, $\Sigma(r)$, will create a shear that is proportional to the *surface mass density contrast*, $\Delta\Sigma(r)$:

$$\Delta\Sigma(r) \equiv \overline{\Sigma}(<r) - \overline{\Sigma}(r) = \Sigma_{\rm crit} \times \gamma_t(r). \tag{8}$$

Here, $\overline{\Sigma}(<r)$ is the mean surface density within proper radius r, $\overline{\Sigma}(r)$ is the azimuthally averaged surface density at radius r (e.g., Miralda-Escude 1991; Wilson et al. 2001), and γ_t is the tangentially projected shear. The geometry of the lens–source system intervenes through the *critical surface mass density*,[20] $\Sigma_{\rm crit}$, which depends on the angular diameter distances to the lens ($D_{\rm OL}$), to the source ($D_{\rm OS}$), and between the lens and source ($D_{\rm LS}$):

$$\Sigma_{\rm crit} = \frac{c^2}{4\pi\, G_{\rm N}} \frac{D_{\rm OS}}{D_{\rm OL}\, D_{\rm LS}}\, , \tag{9}$$

where $G_{\rm N}$ represents Newton's constant. Hence, if redshift information is available for every lens–source pair, each estimate of γ_t can be directly converted to an estimate of $\Delta\Sigma(r)$ which is a more desirable quantity than γ_t because it depends only on the mass distribution of the lens.

To measure $\Delta\Sigma(r)$ with high S/N, the lensing signal must be stacked over many foreground lenses and background sources. For every ith lens and jth source separated by a proper distance r_{ij}, an estimator of the mean excess projected surface mass density ($\Delta\tilde{\Sigma}_{ij}$) at r_{ij} is computed according to

$$\Delta\tilde{\Sigma}_{ij}(r_{ij}) = \tilde{\gamma}_{t,ij} \times \Sigma_{{\rm crit},ij}, \tag{10}$$

where $\tilde{\gamma}_{t,ij}$ is the tangential shear of the source relative to the lens. The COSMOS photometric redshifts described in Section 2.2 are used to estimate $\Sigma_{{\rm crit},ij}$ for every lens–source pair. In order to optimize the S/N, an inverse variance weighting scheme is employed when $\Delta\Sigma_{ij}$ is summed over many lens–source pairs. Each lens–source pair is attributed a weight that is equal to the estimated variance of the measurement:

$$w_{ij} = \frac{1}{(\Sigma_{{\rm crit},ij} \times \sigma_{\tilde{\gamma},ij})^2}. \tag{11}$$

---

[19] Not to be confused with Newton's constant which we have noted $G_{\rm N}$.

[20] Note that some authors define the comoving critical surface mass density which has an extra factor of $(1+z)^{-2}$ with respect to ours due to the use of comoving instead of physical distances.

Table 3
Binning Scheme for the g–g Lensing

	Limits	g–g bin1	g–g bin2	g–g bin3	g–g bin4	g–g bin5	g–g bin6	g–g bin7
$z_1 = [0.22, 0.48]$	min $\log_{10}(M_*)$	11.12	10.89	10.64	10.3	9.82	9.2	8.7
	max $\log_{10}(M_*)$	12.0	11.12	10.89	10.64	10.3	9.8	9.2
$z_2 = [0.48, 0.74]$	min $\log_{10}(M_*)$	11.29	11.05	10.88	10.65	10.3	9.8	9.3
	max $\log_{10}(M_*)$	12.0	11.29	11.05	10.88	10.65	10.3	9.8
$z_3 = [0.74, 1.0]$	min $\log_{10}(M_*)$	11.35	11.16	10.97	10.74	10.39	9.8	none
	max $\log_{10}(M_*)$	12.0	11.35	11.16	10.97	10.74	10.39	none

In this manner, faint small galaxies which have large measurement errors are downweighted with respect to sources that have well-measured shapes.

For the types of lenses studied in this paper, the S/N per lens is not high enough to measure $\Delta\Sigma$ on an object-by-object basis so instead we stack the signal over many lenses. For a given sample of lenses, the total excess projected surface mass density is the weighted sum over all lens–source pairs:

$$\Delta\Sigma = \frac{\sum_{j=1}^{N_{\text{Lens}}} \sum_{i=1}^{N_{\text{Source}}} w_{ij} \times \tilde{\gamma}_{t,ij} \times \Sigma_{\text{crit},ij}}{\sum_{j=1}^{N_{\text{Lens}}} \sum_{i=1}^{N_{\text{Source}}} w_{ij}}. \quad (12)$$

3.5. Galaxy–Galaxy Lensing Measurements

We only give a brief outline of the overall methodology used to compute the g–g lensing signals since this has already been presented in detail in Leauthaud et al. (2010). Foreground lens galaxies are divided into three redshift samples and then are further binned by stellar mass (see Figure 2 and Table 3). For each lens sample, $\Delta\Sigma$ is computed according to Equation (12) from 25 kpc (physical distance) to 1.5 Mpc in logarithmically spaced radial bins of 1.8 dex. In Leauthaud et al. (2010), we used a theoretical estimate of the shape measurement error in order to derive the inverse variance for each source galaxy. Instead, in this paper, the dispersion of each shear component is measured directly from the data in bins of S/N and magnitude. The measured shear dispersion is equal to the quadratic sum of the intrinsic shape noise and of the shape measurement error (Equation (6)). Our empirical derivation of the shear dispersion varies from $\sigma_{\tilde{\gamma}} \sim 0.25$ for bright galaxies with high S/N to $\sigma_{\tilde{\gamma}} \sim 0.4$ for faint galaxies with low S/N. Overall, we find that the theoretical and the empirical schemes yield very similar results with the latter method resulting in slightly larger error bars because the theoretical scheme tends to somewhat underestimate the shape measurement error for faint galaxies.

Photometric redshifts are used to derive Σ_{crit} for each lens–source pair. The lower 68% confidence bound on each source redshift is used to select background galaxies. For each lens–source pair, we demand that $z_{\text{source}} - z_{\text{lens}} > \sigma_{68\%}(z_{\text{source}})$ so as to minimize foreground contamination. The g–g lensing signal is most sensitive to redshift errors when z_{source} is only slightly larger then z_{lens} (see Figure 1). For this reason, in addition to the previous cut, we also implement a fixed cut so that $z_{\text{source}} - z_{\text{lens}} > 0.1$. Furthermore, in order to minimize the effects of signal dilution caused by catastrophic errors, we also reject all source galaxies with a secondary peak in the redshift probability distribution function (i.e., the parameter z_{P2} is non zero in the Ilbert et al. 2009 catalog). This cut is aimed to reduce the number of catastrophic errors in the source catalog. After all cuts have been applied, the g–g lensing source catalog that we use represents 35 galaxies per arcmin^2.

Finally, we re-compute all our g–g lensing signals using the Schrabback et al. (2010) COSMOS shear catalog which has been independently derived from ours. We find identical g–g lensing signals from both shear catalogs, indicating that any relative shear calibration differences between the two shear catalogs has no impact on these results. This test provides an independent validation of our g–g lensing results.

4. THEORETICAL FRAMEWORK

Paper I presents the general theoretical foundations that form the backbone of this paper. In this section, we only give a brief, and thus necessarily incomplete, review of the theoretical background and strongly encourage the reader to refer to Paper I for further details. We adopt the same model and notation as in Paper I.

Paper I describes an HOD-based model that can be used to analytically predict the SMF, g–g lensing, and clustering signals. The key component of this model is the SHMR which is modeled as a log-normal probability distribution function with a log-normal scatter[21] denoted $\sigma_{\log M_*}$, and with a mean–log relation denoted as $M_* = f_{\text{SHMR}}(M_h)$.

For a given parameter set and cosmology, f_{SHMR} and $\sigma_{\log M_*}$ can be used to determine the central and satellite occupation functions, $\langle N_{\text{cen}}\rangle$ and $\langle N_{\text{sat}}\rangle$. These are used in turn to predict the SMF, g–g lensing, and clustering signals.

4.1. The Stellar-to-halo Mass Relation

Following Behroozi et al. (2010, hereafter B10), $f_{\text{SHMR}}(M_h)$ is mathematically defined via its inverse function:

$$\log_{10}\left(f_{\text{SHMR}}^{-1}(M_*)\right) = \log_{10}(M_h)$$
$$= \log_{10}(M_1) + \beta \log_{10}\left(\frac{M_*}{M_{*,0}}\right)$$
$$+ \frac{\left(\frac{M_*}{M_{*,0}}\right)^{\delta}}{1 + \left(\frac{M_*}{M_{*,0}}\right)^{-\gamma}} - \frac{1}{2}, \quad (13)$$

where M_1 is a characteristic halo mass, $M_{*,0}$ is a characteristic stellar mass, β is the low-mass slope, and δ and γ control the high-mass slope. We refer to B10 for a more detailed justification of this functional form. Briefly, we expect that at least four parameters are required to model the SHMR: a normalization, break, a low-mass slope, and a bright end slope. In addition, B10 have found that the SHMR displays sub-exponential behavior at large M_*. This is modeled by the δ parameter which leads to a total of five parameters. Figure 3 illustrates the influence of

---

[21] Scatter is quoted as the standard deviation in the logarithm base 10 of the stellar mass at fixed halo mass.
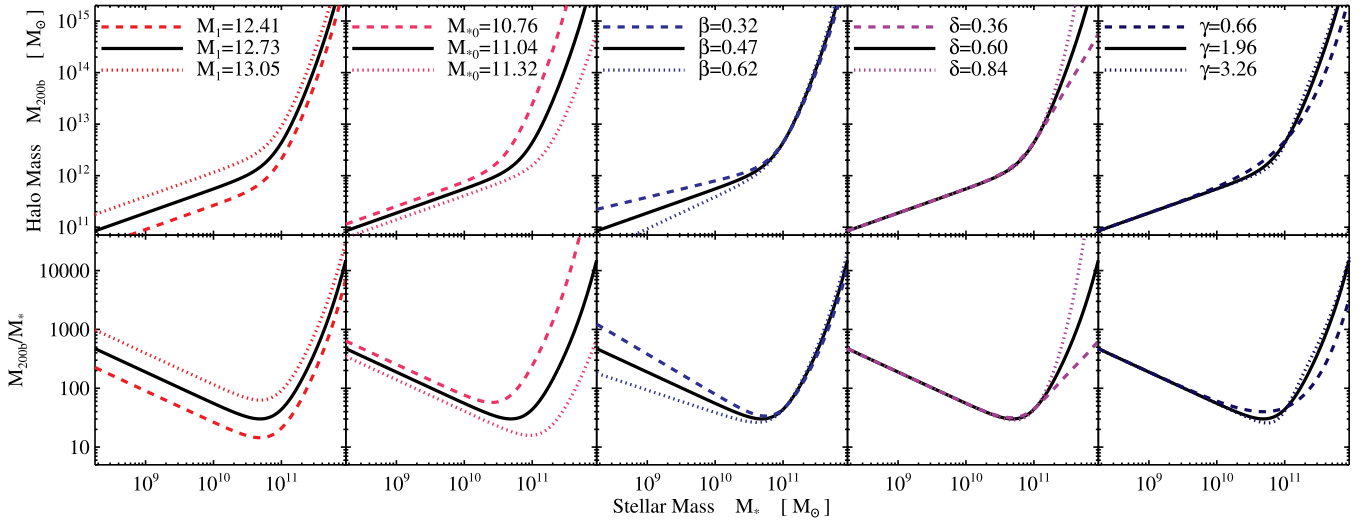
Figure 3. Illustration of the influence of M_1, $M_{*,0}$, β, δ, and γ on the shape of the SHMR.
(A color version of this figure is available in the online journal.)

each parameter on the shape on the SHMR and further details on the role of each parameter can be found in Section 2.1 of Paper I.

In contrast to B10, we do not parameterize the redshift evolution of this functional form. Rather, we bin the data into three redshift bins and check for redshift evolution in the parameters a posteriori. We also assume that Equation (13) is only relevant for central galaxies. Following the HOD ansatz, satellite galaxies within groups and clusters occupy subhalos—bound, virialized halos that are contained within the radius of a larger halo. Abundance matching models like B10 assume that the halos and subhalos of the same mass (or circular velocity) contain galaxies of the same stellar mass, where the subhalo mass is taken as the mass at the last time the galaxy was a central galaxy. Here we put no such prior on the galaxy–subhalo connection. Rather, the halo occupation of satellite galaxies is constrained by the data.

4.2. Scatter between Stellar and Halo Mass

The measured scatter in stellar mass at fixed halo mass has an intrinsic component (denoted $\sigma^{i}_{\log M_*}$), but also includes a stellar mass measurement error due to redshift, photometry, and modeling uncertainties (denoted $\sigma^{m}_{\log M_*}$). Ideally, we would measure both components but unfortunately we can only constrain the quadratic sum of these two sources of scatter. Nonetheless, given a model for $\sigma^{m}_{\log M_*}$, we could in principle extract $\sigma^{i}_{\log M_*}$ from $\sigma_{\log M_*}$.

Previous work suggests that $\sigma_{\log M_*}$ is independent of halo mass. For example, Yang et al. (2009) find that $\sigma_{\log M_*} = 0.17$ dex and More et al. (2009) find a scatter in luminosity at fixed halo mass of 0.16 ± 0.04 dex. Both Moster et al. (2010) and B10 are able to fit the Sloan Digital Sky Survey (SDSS) galaxy SMF assuming $\sigma_{\log M_*} = 0.15$ dex and $\sigma_{\log M_*} = 0.175$ dex, respectively. However, these results are derived with spectroscopic samples of galaxies. In contrast to these surveys, we expect a larger measurement error for the COSMOS stellar masses due to the use of photometric redshifts. In addition, since photo-z errors increase for fainter galaxies, we might also expect that $\sigma^{m}_{\log M_*}$ (and thus $\sigma_{\log M_*}$) will depend on M_*.

To test if the assumption that $\sigma_{\log M_*}$ is constant with M_* has any impact on our results, we implement two models for $\sigma_{\log M_*}$.

In the first case (called "SIG_MOD1"), $\sigma_{\log M_*}$ is assumed to be constant (this is our base-line model). In the second case (called "SIG_MOD2"), we explicitly model $\sigma^{m}_{\log M_*}$ to reflect stellar mass measurement errors. Note that the goal of this exercise is not to perform a careful and thorough error analysis, but simply to build a realistic enough model to asses whether or not an M_*-dependent error has any strong impact on our conclusions.

For the SIG_MOD2 model, we consider three contributions to the stellar mass error budget. The first is called "model error": this is measured by the 68% confidence interval of the mass probability distribution determined for each galaxy by the mass estimator. It represents the range of model templates (each with its own M/L ratio) that provide reasonable fits to the observed SED. This range is determined by the photometric uncertainty in the observed SED, degeneracies in the grid of models used to fit the data, and how well the grid of models represents the true parameter space of observed galaxy populations as well as their colors.[22] The second term is the photo-z error, which derives from the uncertainty in the luminosity distance owing to the error on a given photometric redshift. The final component is the photometric uncertainty from the observed K-band magnitude, which translates into an uncertainty in luminosity and therefore stellar mass. The total measurement error, $\sigma^{m}_{\log M_*}$, is the sum in quadrature of these three sources of error. The results are shown in Figure 4 for the three redshift bins.

As detailed in Section 5, we find that our results are largely unchanged, regardless of which form we adopt for $\sigma_{\log M_*}$. This can be explained as follows. Since the data are binned by M_*, the observables are in fact sensitive to the scatter in halo mass at fixed stellar mass, denoted $\sigma_{\log M_h}$. Given a model for the SHMR, $\sigma_{\log M_h}$ can be mathematically derived from $\sigma_{\log M_*}$. Further details on the mathematical connection between $\sigma_{\log M_*}$ and $\sigma_{\log M_h}$ can be found in Paper I. We find that the slope of the SHMR increases steeply at $M_* > 10^{11}\ M_\odot$ so that $\sigma_{\log M_h}$ becomes quite large at the high-mass end. For example, $\sigma_{\log M_h} \sim 0.46$ dex at $M_* = 10^{11}\ M_\odot$ and $\sigma_{\log M_h} \sim 0.7$ dex at $M_* = 10^{11.5}\ M_\odot$. As a result, the data are particularly

---

[22] Model template problems, especially in the rest-frame near-IR, and age–metallicity degeneracies may help explain the slight rise in the "model error" contribution to the total stellar mass uncertainty for high-mass galaxies at low redshift in Figure 4.
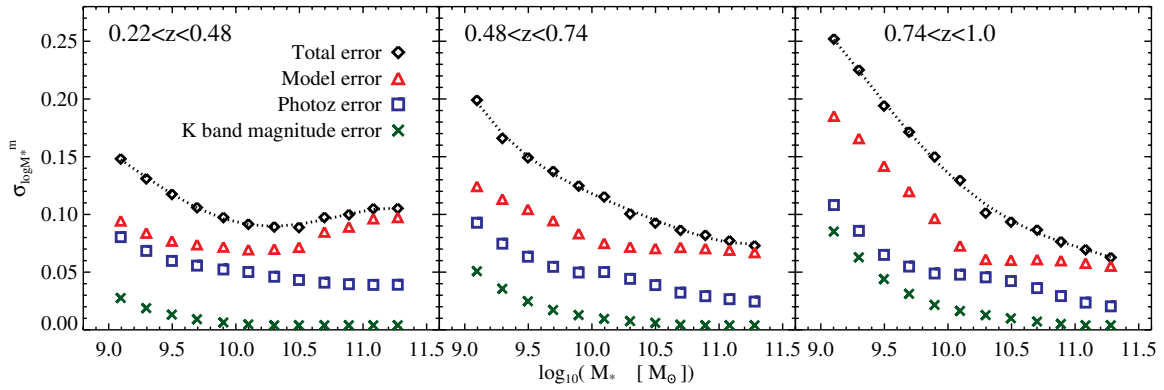
Figure 4. Three sources of error that contribute to $\sigma_{\log M_*}^{\mathrm{m}}$ for the SIG_MOD2 model. At all redshifts, $\sigma_{\log M_*}^{\mathrm{m}}$ is dominated by model error followed by photo-z error and finally by K-band magnitude error. The rise in the total error at high masses in the low-z bin is caused by the model error term. This is likely a result of degeneracies and template errors in the parameter space of models that provide reasonable fits to the early-type SEDs which dominate the high-mass end at low redshift. Indeed, the estimated stellar mass probability distribution functions at high mass in the low-z bin tend to show more bi-modality. The difference in error across the full mass range from this effect is small however, corresponding to only 0.03 dex.

(A color version of this figure is available in the online journal.)

sensitive to $\sigma_{\log M_*}$ at large M_* but not very sensitive to $\sigma_{\log M_*}$ at low M_*. Therefore, accounting for the mass dependence of $\sigma_{\log M_*}$ has little impact on the results because the constraints on $\sigma_{\log M_*}$ mainly originate from high-mass galaxies anyway.

Finally, we note that our derived values for the parameters of the SHMR should be independent of $\sigma_{\log M_*}$ (we will show that $\sigma_{\log M_*}$ is not largely degenerate with any of the other nine parameters in Section 5). The observables (g–g lensing, clustering, and SMF) do themselves depend on $\sigma_{\log M_*}$ but since we account for $\sigma_{\log M_*}$ in the model, the extracted SHMR should reflect the true underlying physical relationship between halo and stellar mass (this however would *not* be the case if one were to neglect $\sigma_{\log M_*}$). In other terms, our model fully accounts for Eddington bias in all three observables (also see discussion in Paper I).

4.3. Parameters in the Model

To model the central occupation function, we use five free parameters ($M_1, M_{*,0}, \beta, \delta, \gamma$) to model f_{SHMR} and we leave $\sigma_{\log M_*}$ as an additional free parameter. As described in Paper I, the central occupation function for a sample of galaxies more massive than M_*^{t1} (where M_*^{t1} represents some threshold in M_*) is expressed as

$$
\begin{aligned}
&\langle N_{\mathrm{cen}}(M_h | M_*^{t1}) \rangle \\
&= \frac{1}{2} \left[1 - \mathrm{erf} \left(\frac{\log_{10}(M_*^{t1}) - \log_{10}(f_{\mathrm{SHMR}}(M_h))}{\sqrt{2}\sigma_{\log M_*}} \right) \right].
\end{aligned}
\tag{14}
$$

Our model also has an additional five parameters that are necessary to model the satellite occupation function, $\langle N_{\mathrm{sat}} \rangle$. For a set of galaxies more massive than threshold M_*^t, $\langle N_{\mathrm{sat}} \rangle$ is

$$
\langle N_{\mathrm{sat}}(M_h | M_*^t) \rangle = \langle N_{\mathrm{cen}}(M_h | M_*^t) \rangle \left(\frac{M_h}{M_{\mathrm{sat}}} \right)^{\alpha_{\mathrm{sat}}} \exp \left(\frac{-M_{\mathrm{cut}}}{M_h} \right).
\tag{15}
$$

The free parameters that determine satellite occupation as a function of stellar mass are $\beta_{\mathrm{sat}}, B_{\mathrm{sat}}, \beta_{\mathrm{cut}}, B_{\mathrm{cut}}$, and α_{sat}. The first two parameters, β_{sat} and B_{sat}, determine the amplitude of $\langle N_{\mathrm{sat}} \rangle$. The second two parameters, β_{cut} and B_{cut}, set the scale

of the exponential cutoff. These parameters enter into $\langle N_{\mathrm{sat}} \rangle$ as

$$
\frac{M_{\mathrm{sat}}}{10^{12} M_\odot} = B_{\mathrm{sat}} \left(\frac{f_{\mathrm{SHMR}}^{-1}(M_*^{t_1})}{10^{12} M_\odot} \right)^{\beta_{\mathrm{sat}}},
\tag{16}
$$

and

$$
\frac{M_{\mathrm{cut}}}{10^{12} M_\odot} = B_{\mathrm{cut}} \left(\frac{f_{\mathrm{SHMR}}^{-1}(M_*^{t_1})}{10^{12} M_\odot} \right)^{\beta_{\mathrm{cut}}}.
\tag{17}
$$

Finally, α_{sat} represents the power-law slope of the satellite mean occupation function. We set $\alpha_{\mathrm{sat}} = 1$ for all samples which should be a good choice because the theoretical expectation is that the number of sub-halos above a given mass scales linearly with halo mass (Kravtsov et al. 2004; Conroy et al. 2006; Moster et al. 2010; Tinker et al. 2010). Results from group catalogs also indicate that $\alpha_{\mathrm{sat}} \sim 1$ (Collister & Lahav 2005; Yang et al. 2009). Previous HOD analyses of clustering results at varying redshifts also vary little from a value of unity (Zehavi et al. 2005, 2011b; Zheng et al. 2007; van den Bosch et al. 2007; Tinker et al. 2007).

In total, our model contains ten free parameters and one fixed parameter (α_{sat}). A summary and description of these parameters can be found in Table 4 and also in Paper I.

4.4. Covariance Matrices

The COSMOS survey covers a relatively small volume and therefore sample variance effects must be taken into account. The volumes probed in the three redshift bins are given in Table 1 and vary from 0.88×10^6 Mpc^3 for the ACS region in z_1 ($0.22 < z < 0.48$) to 4.39×10^6 Mpc^3 for the Subaru region in z_3 ($0.74 < z < 1.0$). The volumes sampled by COSMOS are too small to obtain an accurate estimate of the sample variance from the data itself.

A series of mock catalogs are used to calculate the covariance matrices for all three observables. Details regarding the construction of these mocks can be found in Paper I. Briefly, COSMOS-like mocks are created from a single simulation (named "Consuelo") 420 h^{-1} Mpc on a side, resolved with 1400^3 particles, and a particle mass of 1.87×10^9 $h^{-1} M_\odot$.[23] This simulation can robustly resolve halos with masses above

---

[23] In this paragraph, numbers are quoted for $H_0 = 100$ h km s^{-1} Mpc^{-1}.

Table 4
Parameters in Model

Parameter	Unit	Description	$\langle N_{\rm cen} \rangle$ or $\langle N_{\rm sat} \rangle$	Free/Fixed
M_1	$M_\odot$	Characteristic halo mass in the SHMR	$\langle N_{\rm cen} \rangle$	Free
$M_{*,0}$	$M_\odot$	Characteristic stellar mass in the SHMR	$\langle N_{\rm cen} \rangle$	Free
β	None	Low-mass slope in the SHMR	$\langle N_{\rm cen} \rangle$	Free
δ	None	Controls high-mass slope in the SHMR	$\langle N_{\rm cen} \rangle$	Free
γ	None	Controls the transition regime in the SHMR	$\langle N_{\rm cen} \rangle$	Free
$\sigma_{\log M_*}$	dex	Log-normal scatter in stellar mass at fixed halo mass	$\langle N_{\rm cen} \rangle$	Free
$\beta_{\rm sat}$	None	Slope of the scaling of $M_{\rm sat}$	$\langle N_{\rm sat} \rangle$	Free
$B_{\rm sat}$	None	Normalization of the scaling of $M_{\rm sat}$	$\langle N_{\rm sat} \rangle$	Free
$\beta_{\rm cut}$	None	Slope of the scaling of $M_{\rm cut}$	$\langle N_{\rm sat} \rangle$	Free
$B_{\rm cut}$	None	Normalization of the scaling of $M_{\rm cut}$	$\langle N_{\rm sat} \rangle$	Free
$\alpha_{\rm sat}$	None	Power-law slope of the satellite occupation function	$\langle N_{\rm sat} \rangle$	Fixed at 1

$\sim 10^{11} \, h^{-1} M_\odot$ and is part of the Las Damas suite[24] (J. McBride et al., in preparation). We create mocks for the three redshift intervals: $z_1 = [0.22, 0.48]$, $z_2 = [0.48, 0.74]$, and $z_3 = [0.74, 1]$. For each redshift interval, we construct a series of mocks created from random lines of sight through the simulation volume that have the same area as COSMOS and the same comoving length for the given redshift slice. This yields 405 independent mocks for the z_1 bin, 172 mocks for the z_2 bin, and 109 mocks for the z_3 bin. For each redshift bin, mocks are created from the simulation output at the median redshift of the bin (see Table 1).

We converge on the mocks used for estimating errors using an iterative method. To begin with, we find an initial best-fit model to the data, without using any covariance matrices. This initial fit is used to populate the mocks and to create a first set of covariance matrices. We then re-fit the data using these covariance matrices and use the best-fit HOD models to create our final covariance matrices. All results presented here use this final set of covariance matrices.

5. RESULTS

We now present the results of fitting the model described in Paper I to the observed COSMOS g–g lensing, clustering, and SMFs.

5.1. Constraining the Model

In order to fit the model to the data, we minimize

$$\chi^2_{\rm tot} = \chi^2_{\Phi_{\rm SMF}} + \sum_i \chi^2_{\Delta\Sigma, i} + \sum_j \chi^2_{w(\theta), j}, \qquad (18)$$

where the sum over i and j indicates summation over the different stellar mass bins and thresholds, respectively. For the SMF and each stellar mass sample in $w(\theta)$ and $\Delta\Sigma$, χ^2 is calculated by

$$\chi^2 = \sum_{n,l} (x_n - y_n) \, C^{-1}_{nl} \, (x_l - y_l), \qquad (19)$$

where x_n is the model calculation of the quantity for data point n, y_n is the measurement, and C^{-1} is the inversion of the covariance matrix.

To obtain the posterior probability distributions for the parameter set $(M_1, M_{*,0}, \beta, \delta, \gamma, \sigma_{\log M_*}, \beta_{\rm sat}, B_{\rm sat}, \beta_{\rm cut}, B_{\rm cut})$, we implement a Markov Chain Monte Carlo (MCMC) algorithm as follows.

1. We sample the region of interest around the best fit by initializing all chains close to the minimum χ^2 solution with varying initial random spreads.
2. We apply conservative limits on all 10 parameters. As shown in Figure 8, the recovered posterior distributions are independent of these limits.
3. The covariance matrix is updated for the first 3000 elements in the chain, and then held fixed for the remainder of the chain.
4. We run six chains per case, with $\sim 40{,}000$ steps. We discard all elements before the covariance matrix is constant (the first 3000), leaving $\sim 37{,}000$ elements per chain.
5. We use the GetDist package provided with CosmoMC (Lewis & Bridle 2002) for computing convergence diagnostics. The chains are tested for convergence and mixing with the Gelman–Rubin criterion (Gelman & Rubin 1992; Gilks et al. 1996). We impose a limit on the worst $R - 1$ statistic of $R - 1 < 0.01$ and observe that for all cases under study the mean and marginalized posterior distributions are well constrained.
6. We use GetDist output statistics to estimate confidence limits on all parameters.

5.2. Fits to the Data

Figures 5–7 show the best-fit models for each of the three redshift bins for the galaxy clustering, the g–g lensing, and the SMF. The upper panels show the angular correlation function $w(\theta)$ for stellar mass threshold samples. The middle right panel shows the COSMOS SMF which is measured for all galaxies with $M_* > 10^{8.7} \, M_\odot$ for z_1, $M_* > 10^{9.3} \, M_\odot$ for z_2, and $M_* > 10^{9.8} \, M_\odot$ for z_3. The dotted blue line shows the SMF of satellite galaxies from our model. The lower panels show the g–g lensing signals for the stellar mass bins defined in Table 3. When looking at Figures 5–7, one must keep in mind that the data points are correlated (see Paper I for the covariance matrices) and so it is difficult to evaluate "by eye" whether or not the fits are adequate. The reduced χ^2 for the fits are 1.7, 1.6, and 1.9 for z_1, z_2, and z_3, respectively.

For our z_1 sample, we have compared the COSMOS mass function with previously published mass functions from SDSS (Li & White 2009; Baldry et al. 2008; Panter et al. 2007). Because of the use of photometric redshifts in COSMOS, we expect a larger stellar mass measurement error which should cause Eddington bias and lead to an inflated observed SMF at the high-mass end in COSMOS compared to SDSS. A more in-depth comparison of the mass functions is discussed further in Section 5.6.

---

[24] Further details regarding this simulation can be found at
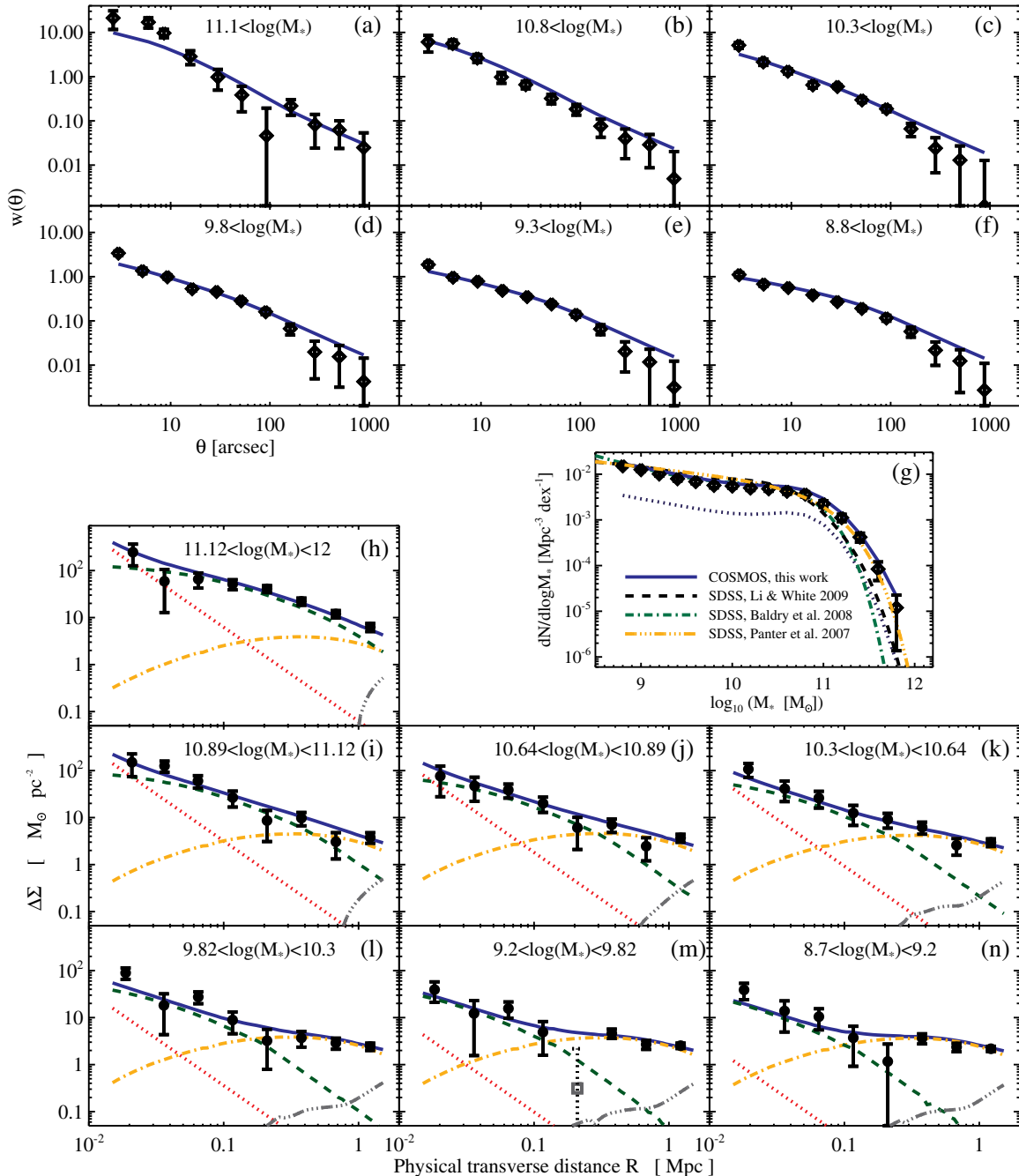http://lss.phy.vanderbilt.edu/lasdamas/simulations.html

Figure 5. Best-fit model for the z_1 ($0.22 < z < 0.48$) redshift bin (blue solid line). Panels (a)–(f): amplitude of the angular correlation function w as a function of angular separation θ (in arcseconds) in stellar mass thresholds. Note that in this redshift bin, the amplitude of w at large separations is artificially deflated by integral constraint (but this is accounted for in the fitted model). Panel (g): COSMOS SMF for $M_* > 10^{8.7}\ M_\odot$ (completeness limit for this redshift bin). For reference, in panel (f), we also show the SDSS mass functions from Li & White (2009) (triple Schechter fit, black dashed line), Baldry et al. (2008) (green dash-dotted line), and from Panter et al. (2007) (orange, dash-dotted line). The dotted blue line in panel (g) shows the SMF of satellite galaxies for the best-fit model. Panels (h)–(n): galaxy–galaxy lensing signal in stellar mass bins. Note that in panel (m), there is a negative data point represented by a gray square (this can occur due to noise and is not a concern). The lensing signal is decomposed into four components: the baryonic term (red dotted line), the central one-halo term (green dashed line), the satellite one-halo term (orange dash-dotted), and the two-halo term (gray triple-dot-dashed line).

(A color version of this figure is available in the online journal.)

5.3. Parameter Constraints and Redshift Evolution

Table 5 gives the best-fit values from `GetDist` for all 10 parameters and for the three redshift bins. Figure 8 shows the one-dimensional and two-dimensional joint marginalized constraints on the parameters for the z_2 bin. All of the parameters have well-behaved, uni-modal distributions. In the interest of

brevity, we have not included equivalent figures for z_1 and z_3 but they are similar to Figure 8. All parameters are well constrained in the three redshift bins.

Table 5 lists the best-fit values for SIG_MOD1 where we have assumed that $\sigma_{\log M_*}$ is constant and for SIG_MOD2 where we have explicitly accounted for stellar mass-dependent errors. We find no strong difference in our results, regardless of which model we
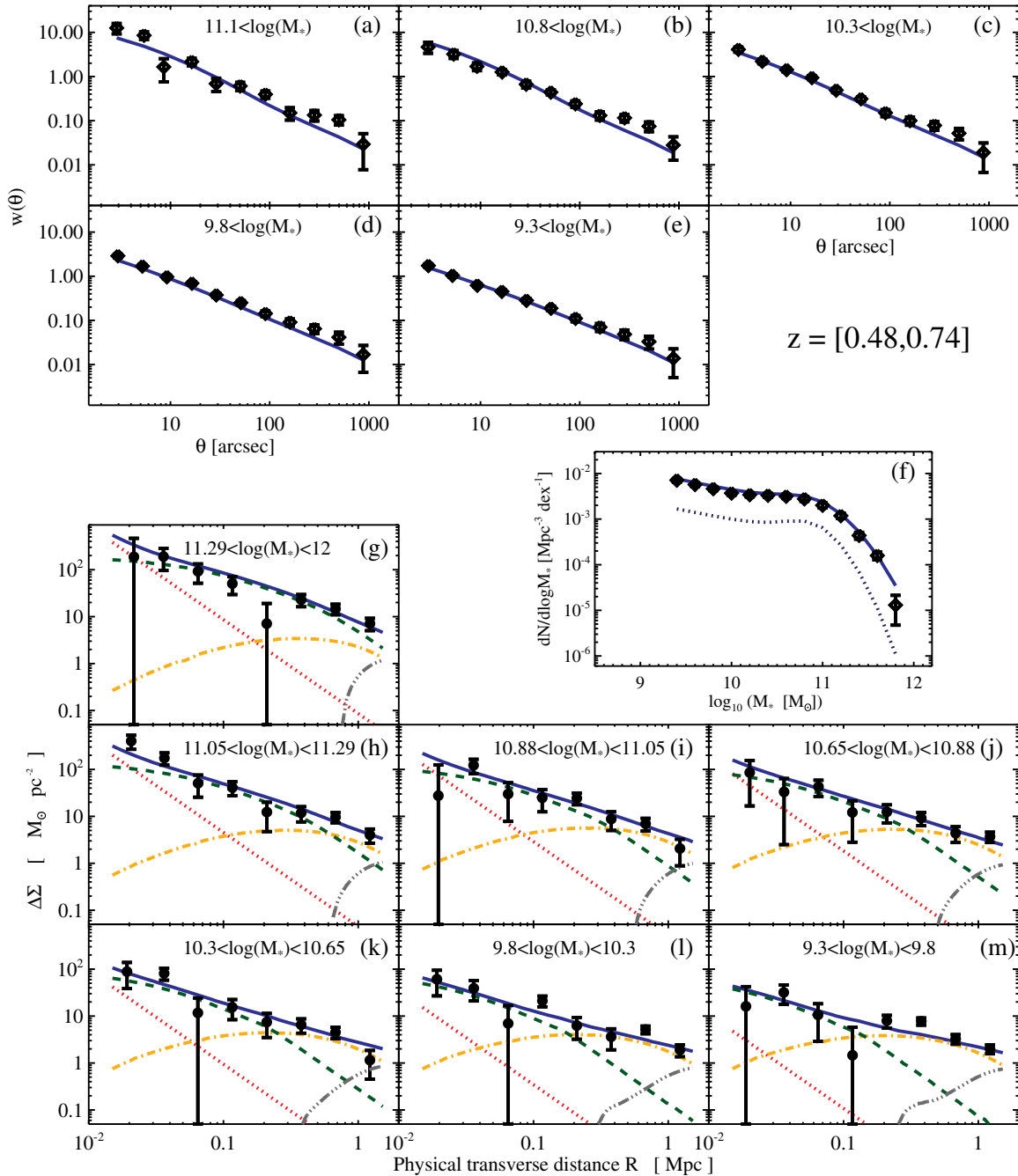
Figure 6. Same as Figure 5 but for the second redshift bin, z_2. Panels (a)–(e): angular correlation function. The angular correlation function is less affected by integral constraint in this redshift bin since the volume probed is 2.3 times larger than z_1. Panel (f): COSMOS SMF for $M_* > 10^{9.3} \, M_\odot$. The dotted blue line in panel (f) shows the SMF of satellite galaxies for the best-fit model. Panels (g)–(m): galaxy–galaxy lensing signal.

(A color version of this figure is available in the online journal.)

adopt. We conclude that our results are robust to the effects of mass-dependent scatter. In the SIG_MOD2 case, we model $\sigma^m_{\log M_*}$ and assume that $\sigma_{\log M_*}$ is the sum in quadrature of $\sigma^i_{\log M_*}$ (which is assumed to be constant) and $\sigma^m_{\log M_*}$. Therefore, the quantity that we actually fit for in the SIG_MOD2 case is $\sigma^i_{\log M_*}$ (whereas in SIG_MOD1 we fit for $\sigma_{\log M_*}$). This is why, as expected, the best-fit scatter in Table 5 is slightly lower for SIG_MOD2 compared to SIG_MOD1. Note that we are not claiming to actually extract meaningful values for the intrinsic scatter in stellar mass at fixed halo mass. To do so would require a more thorough error analysis which is beyond the scope of this paper. Overall, our conclusions

regarding $\sigma_{\log M_*}$ are twofold. First, we can safely assume that $\sigma_{\log M_*}$ is constant and ignore any mass-dependent effects induced by measurement error. This is due to the fact that all three observables are primarily sensitive to the effects of $\sigma_{\log M_*}$ at large M_* where the slope of the SHMR increases sharply. Similar conclusions were reached by B10 who find that the effects of scatter are insignificant below $M_* = 10^{10.5} \, M_\odot$ where the slope of the SHMR is not steep enough to have a significant impact. Second, we find that $\sigma_{\log M_*} \sim 0.23 \pm 0.03$ dex, in broad agreement with previous results. For example, B10 estimate that $\sigma^m_{\log M_*} = 0.07$ dex and $\sigma^i_{\log M_*} = 0.16$ dex, resulting in a total
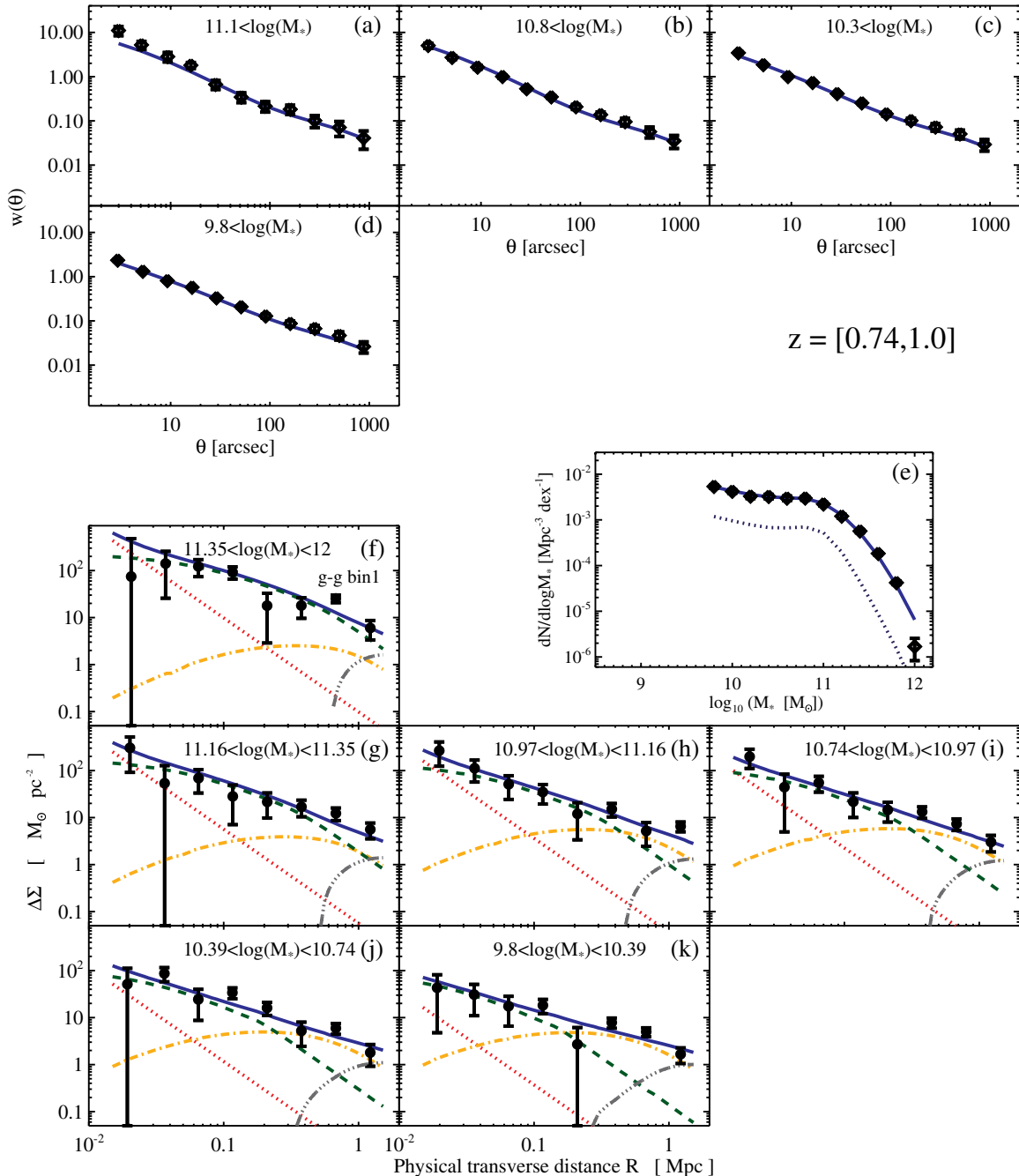
Figure 7. Same as Figure 5 but for the third redshift bin, z_3. Panels (a)–(d): angular correlation function. The angular correlation function is less affected by integral constraint in this redshift bin since the volume probed is five times larger than z_1. Panel (e): COSMOS SMF for $M_* > 10^{9.8} M_\odot$. The dotted blue line in panel (e) shows the SMF of satellite galaxies for the best-fit model. Panels (f)–(k): galaxy–galaxy lensing signal.

(A color version of this figure is available in the online journal.)

scatter of $\sigma_{\log M_*} = 0.175$ dex (their total scatter is lower than ours as expected because we have a larger $\sigma_{\log M_*}^{\mathrm{m}}$ component).

Figure 9 shows the measured redshift evolution for all 10 parameters. Previous work on this topic has been strongly limited by systematic differences in stellar mass estimates between low- and high-z surveys. The main factors that contribute to this systematic uncertainty arise from the choice of an IMF, a stellar population synthesis (SPS) model, a dust model, and a population history model (estimates for the magnitude of each effect can be found in B10). According to B10, the total systematic uncertainty of stellar mass estimates (excluding IMF uncertainties) is of order 0.25 dex. In addition, the choice of an

IMF results in another 0.25 dex uncertainty. We stress that the results in this paper have been derived in a homogeneous fashion from high to low redshift. Our conclusions regarding redshift evolution should thus be more robust than those from work that combine results from distinct low- and high-z surveys. While we believe that a homogeneous analysis globally reduces the systematic errors associated with redshift trends, we should note that our results might still be affected at some level by redshift-dependence systematic errors in stellar mass estimators. These could be caused, for example, by a redshift evolution of the IMF. Currently, however, the magnitude of such redshift-dependence systematic errors is very poorly known. For this reason, we do
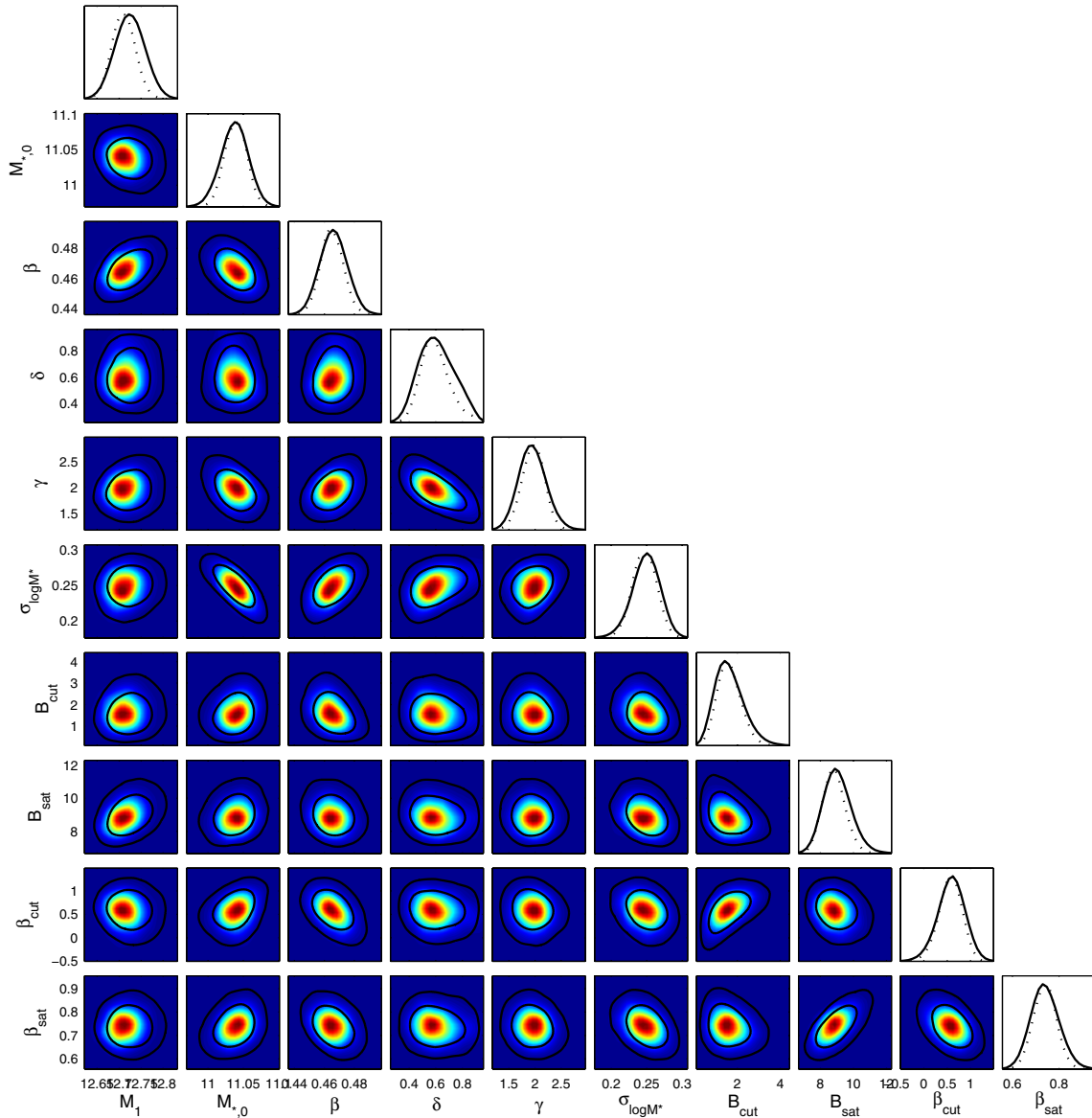
13

Figure 8. One- and two-dimensional joint-mean and marginalized distributions for all 10 parameters for the z_2 bin. Dotted lines in the one-dimensional distributions (and shaded contours in the two-dimensional planes) show mean likelihoods of samples and solid lines show marginalized probabilities. In the two-dimensional planes, blue to red denotes the region of lowest to highest likelihood density. Solid contours in the two-dimensional plane represent the 68% (1σ) and 95% (2σ) confidence regions.

(A color version of this figure is available in the online journal.)

not discuss such errors further in this paper, however, this is clearly an issue that requires further investigation.

The most striking result from Figure 9 is the redshift evolution in the two parameters M_1 and $M_{*,0}$. This is one of the major results of this paper which we will discuss in more detail in the following section. Apart from these two parameters, there is marginal evidence for some evolution in γ and B_{sat}. No strong evolution is detected in the remaining six parameters. It is interesting to note that β (which controls the low-mass slope of the SHMR) remains constant at $\beta \sim 0.46$. We will provide an interpretation of this result in the discussion section.

5.4. The SHMR from $z = 0$ to $z = 1$

Figure 10 shows the best-fit SHMR for z_1 compared to a variety of low-redshift constraints from weak lensing (Mandelbaum

et al. 2006b; Leauthaud et al. 2010; Hoekstra 2007), abundance matching (Moster et al. 2010; Behroozi et al. 2010), satellite kinematics (Conroy et al. 2007; More et al. 2010), and the Tully–Fisher relation (Geha et al. 2006; Pizagno 2006; Springob et al. 2005; Blanton et al. 2008) (see Section 5.5 for a more in-depth comparison). Most of the data are in broad agreement and show clear evidence for a variation in the dark-to-stellar mass ratio with a minimum of $M_h/M_* \sim 27$ at $M_* \sim 4.5 \times 10^{10}\ M_\odot$ and $M_h \sim 1.2 \times 10^{12}\ M_\odot$. As demonstrated by B10, however, meaningful and detailed comparisons between various data sets are hampered by systematic uncertainties in stellar mass estimates. For this reason, we will mainly focus in what follows on the conclusions that can be drawn by inter-comparing the three COSMOS redshift bins.

At low stellar mass, M_h scales as $M_h \propto (M_*)^{0.46}$ and this scaling does not evolve significantly with redshift from $z = 0.2$
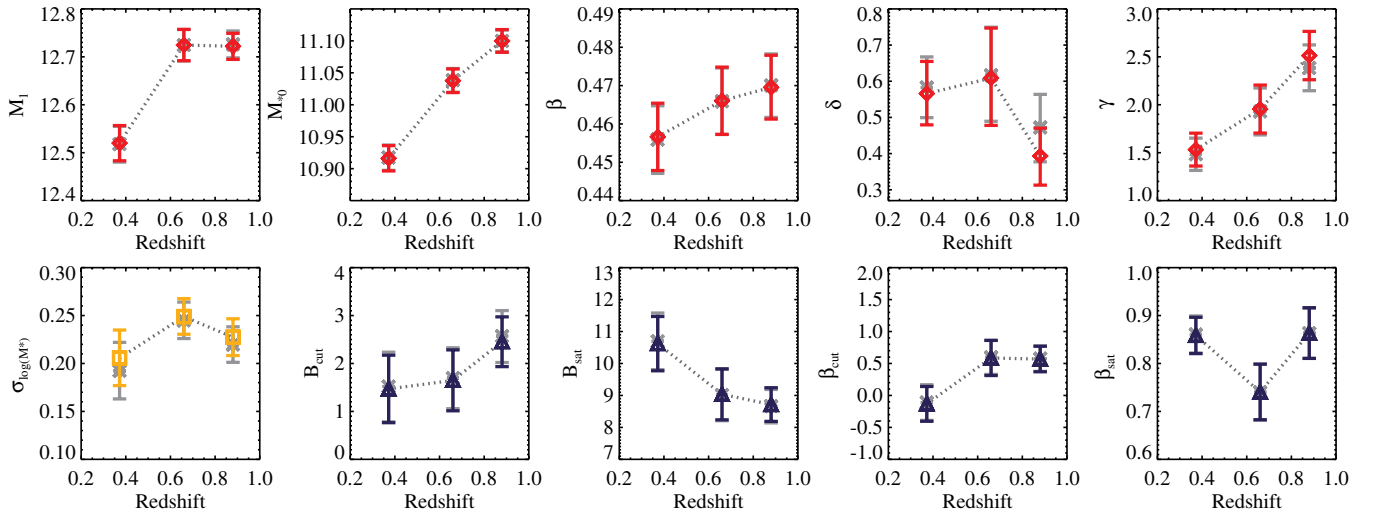
Figure 9. Redshift evolution in the 10 parameters. Red diamonds indicate evolution in the five parameters that describe the SHMR (M_1, $M_{*,0}$, β, δ, γ). Orange squares show the scatter in stellar mass at fixed halo mass ($\sigma_{\log M_*}$). Blue triangles show the remaining four parameters that describe the satellite occupation function ($\beta_{\rm sat}$, $B_{\rm sat}$, $\beta_{\rm cut}$, $B_{\rm cut}$). Gray data points show the best-fit parameters when we assume a stellar mass-dependent scatter due to photometric redshifts (the SIG_MOD2 model).

(A color version of this figure is available in the online journal.)

Table 5
Best-fit Parameters for the Three Redshift Bins

Parameter	$z_1 = [0.22, 0.48]$	$z_2 = [0.48, 0.74]$	$z_3 = [0.74, 1]$
		SIG_MOD1	
$\log_{10}(M_1)$	12.520 ± 0.037	12.725 ± 0.032	12.722 ± 0.027
$\log_{10}(M_{*,0})$	10.916 ± 0.020	11.038 ± 0.019	11.100 ± 0.018
β	0.457 ± 0.009	0.466 ± 0.009	0.470 ± 0.008
δ	0.566 ± 0.086	0.61 ± 0.13	0.393 ± 0.088
γ	1.53 ± 0.18	1.95 ± 0.25	2.51 ± 0.25
$\sigma_{\log M_*}$	0.206 ± 0.031	0.249 ± 0.019	0.227 ± 0.020
$B_{\rm cut}$	1.47 ± 0.73	1.65 ± 0.65	2.46 ± 0.53
$B_{\rm sat}$	10.62 ± 0.87	9.04 ± 0.81	8.72 ± 0.53
$\beta_{\rm cut}$	-0.13 ± 0.28	0.59 ± 0.28	0.57 ± 0.20
$\beta_{\rm sat}$	0.859 ± 0.038	0.740 ± 0.059	0.863 ± 0.053
		SIG_MOD2	
$\log_{10}(M_1)$	12.518 ± 0.038	12.724 ± 0.033	12.726 ± 0.028
$\log_{10}(M_{*,0})$	10.917 ± 0.020	11.038 ± 0.019	11.100 ± 0.017
β	0.456 ± 0.009	0.466 ± 0.009	0.470 ± 0.008
δ	0.582 ± 0.083	0.62 ± 0.12	0.47 ± 0.10
γ	1.48 ± 0.17	1.93 ± 0.25	2.38 ± 0.24
$\sigma_{\log M_*}^i$ [a]	0.192 ± 0.031	0.245 ± 0.019	0.220 ± 0.019
$B_{\rm cut}$	1.52 ± 0.79	1.69 ± 0.65	2.57 ± 0.56
$B_{\rm sat}$	10.69 ± 0.89	9.01 ± 0.81	8.66 ± 0.53
$\beta_{\rm cut}$	-0.11 ± 0.29	0.60 ± 0.27	0.58 ± 0.20
$\beta_{\rm sat}$	0.860 ± 0.039	0.740 ± 0.059	0.863 ± 0.053

Note. [a] In the SIG_MOD2 case we fit for $\sigma_{\log M_*}^i$ whereas in the SIG_MOD1 case we fit for $\sigma_{\log M_*}$.

to $z = 1$. At high stellar mass, the SHMR rises sharply at $M_* > 10^{10.5} M_\odot$ as a result of which $\sigma_{\log M_h}$ (the scatter in halo mass at fixed stellar mass) also increases and M_* is clearly no longer a good tracer of halo mass. For example, a galaxy with $M_* \sim 10^{11.3} M_\odot$ may be the central galaxy of group with $M_h \sim 10^{13}$–$10^{14} M_\odot$ or may also be the central galaxy of a cluster with $M_h > 10^{15} M_\odot$.

A quantity that is of particular interest is the mass at which the ratio M_h/M_* reaches a minimum. This minimum is noteworthy for models of galaxy formation because it marks the mass at

which the accumulated stellar growth of the central galaxy has been the most efficient. We describe the SHMR at this minimum in terms of the "pivot stellar mass," $M_*^{\rm piv}$, the "pivot halo mass," $M_h^{\rm piv}$, and the "pivot ratio," $(M_h/M_*)^{\rm piv}$. Note that $M_*^{\rm piv}$ and $M_h^{\rm piv}$ are not simply equal to M_1 and $M_{*,0}$. Indeed, the mathematical formulation of the SHMR is such that the pivot masses depend on all five parameters. The three parameters that have the strongest effect on the pivot masses are M_1, $M_{*,0}$, and γ (see Paper I).

Figure 11 shows the redshift evolution of the SHMR. Three points are of particular interest in this figure. First, we detect no strong redshift evolution in the low-mass slope of the SHMR ($M_* < 10^{10.2} M_\odot$). Indeed, as highlighted in the previous section already, β is remarkably constant out to $z = 1$. In Paper I, we have shown that β regulates the low-mass slope of the SMF so in other terms, we could also state that the faint end slope of the SMF shows remarkably little redshift evolution. We do however find that the amplitude of the low-mass ($M_* < 10^{10.2} M_\odot$) SHMR was higher at earlier times so that galaxies at fixed stellar mass live in more massive halos at earlier epochs. We will return to this result in the discussion section.

Second, we detect a strong redshift evolution in $M_*^{\rm piv}$ and $M_h^{\rm piv}$ which is shown more explicitly in Figure 12. The detected evolution is such that both the halo mass and the stellar mass for which the accumulated stellar growth of the central galaxy has been the most efficient are smaller at late times than at earlier times. This trend is a manifestation of at least one meaning of the term "downsizing" (Cowie et al. 1996; Brinchmann & Ellis 2000; Juneau et al. 2005). Originally, the term downsizing referred to the notion that the maximum K-band luminosity of galaxies above a specific star formation rate (SSFR) threshold decreases with time (Cowie et al. 1996). Since then, downsizing has been widely employed to more generally describe the behavior in which a certain parameter that regulates galaxy formation decreases with time (for recent discussions on downsizing see Fontanot et al. 2009 and Conroy & Wechsler 2009). Our results show strong evidence for downsizing in both the pivot halo mass and the pivot stellar
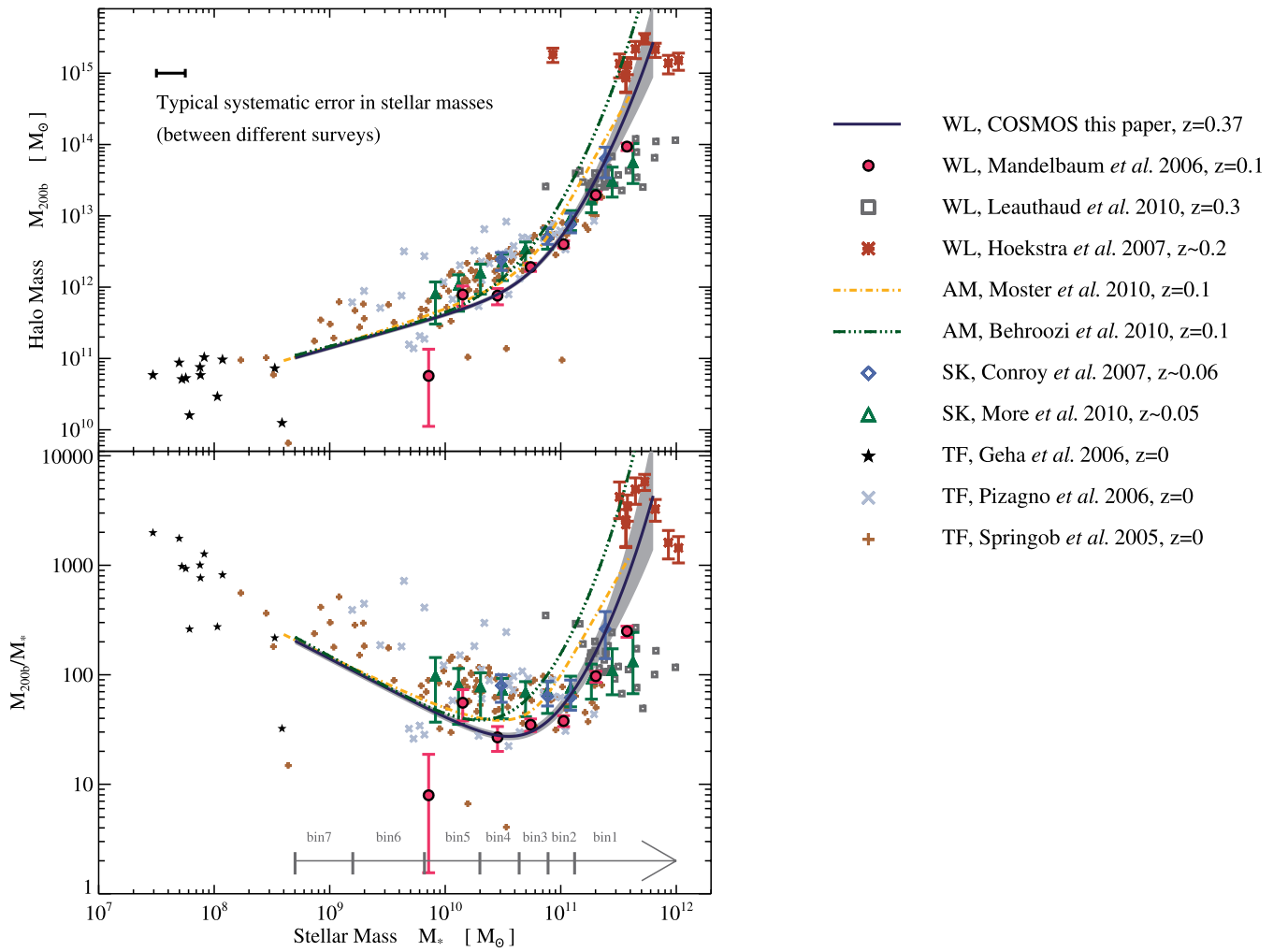
Figure 10. Top panel: inferred SHMR in the z_1 redshift bin compared to other low-redshift measurements from weak lensing (WL), abundance matching (AM), satellite kinematics (SK), and the Tully–Fisher relation (TF). The COSMOS z_1 results are shown by the solid dark blue line and the shaded gray region represents the 1σ error on the SHMR. This SHMR represents $\langle \log_{10}(M_*(M_h)) \rangle$. With the exception of Conroy et al. (2007), all data points either use or have been converted to this same averaging system. Overall, there is a broad agreement between various probes. Detailed comparisons between various data sets, however, are limited by systematic differences in stellar mass estimates due to varying assumptions (e.g., star formation histories, extinction laws, stellar population models). Bottom panel: dark-to-stellar mass ratio as a function of stellar mass. We observe a clear variation in M_{200b}/M_* with M_{200b}/M_* reaching a minimum of $M_h/M_* \sim 27$ at $M_* \sim 4.5 \times 10^{10}\ M_\odot$ and $M_{200b} \sim 1.2 \times 10^{12}\ M_\odot$. The dark-to-stellar mass ratio rises sharply at $M_* > 5 \times 10^{10}\ M_\odot$ so that a cluster of halo mass $M_{200b} \sim 10^{15}\ M_\odot$ will reach a ratio of $M_{200b}/M_* \sim 2000$. Note that this ratio only refers to the ratio between the halo mass and the stellar mass of the *central galaxy*. For example, in the case of clusters, we are comparing the ratio of the cluster halo mass to stellar mass of the central brightest cluster galaxy (BCG).

(A color version of this figure is available in the online journal.)

mass. We have already remarked in the previous section that a strong evolution in M_1 and $M_{*,0}$ is seen in Figure 9. Although these two parameters are not strictly equal to M_*^{piv} and M_h^{piv}, they do have a strong impact on the location of the pivot masses. Thus, the evolution seen in M_1 and $M_{*,0}$ is directly related to the observed downsizing behavior in the pivot masses that is apparent in Figures 11 and 12. The pivot stellar mass evolves from $M_*^{\mathrm{piv}} = 5.75 \pm 0.13 \times 10^{10}\ M_\odot$ at $z = 0.88$ to $M_*^{\mathrm{piv}} = 3.55 \pm 0.17 \times 10^{10}\ M_\odot$ at $z = 0.37$ with an evolution detected at 10σ. We note that all errors have been derived by marginalizing over all other parameters.

The evolution in M_*^{piv} varies smoothly in the three redshift bins, however the evolution in M_h^{piv} is less smooth, in particular in the z_2 bin. We suggest that M_h^{piv} is more sensitive to sample variance than M_*^{piv}. Indeed, the first-order effect of sample variance is to change the normalization of the SMF (see Paper I); this will directly affect M_1 and thus M_h^{piv}. In summary: M_h^{piv} is sensitive to sample variance between redshift bins whereas M_*^{piv}

is sensitive to systematic errors in stellar mass measurements between redshift bins.

Finally, at high masses ($M_* > 10^{11}\ M_\odot$) there is an interesting hint that the amplitude of the SHMR is decreasing at higher redshifts, but we lack the statistics for a clear detection, mainly due to the small volume probed by COSMOS.

5.5. Comparison with Previous Work

Figure 10 compares our z_1 SHMR to previous work on this topic at low redshift. The general picture that emerges from Figure 10 is one of remarkable broad agreement between various methods on the overall shape of the SHMR. In detail, however, meaningful comparison between various surveys is severely limited by systematic differences in stellar mass estimates (~ 0.25 dex between different surveys). For this reason, we mainly focus on qualitative comparisons in this section. All results have been adjusted to our assumed value of $H_0 = 72\ \mathrm{km\ s^{-1}\ Mpc^{-1}}$ and unless stated otherwise, halo masses are
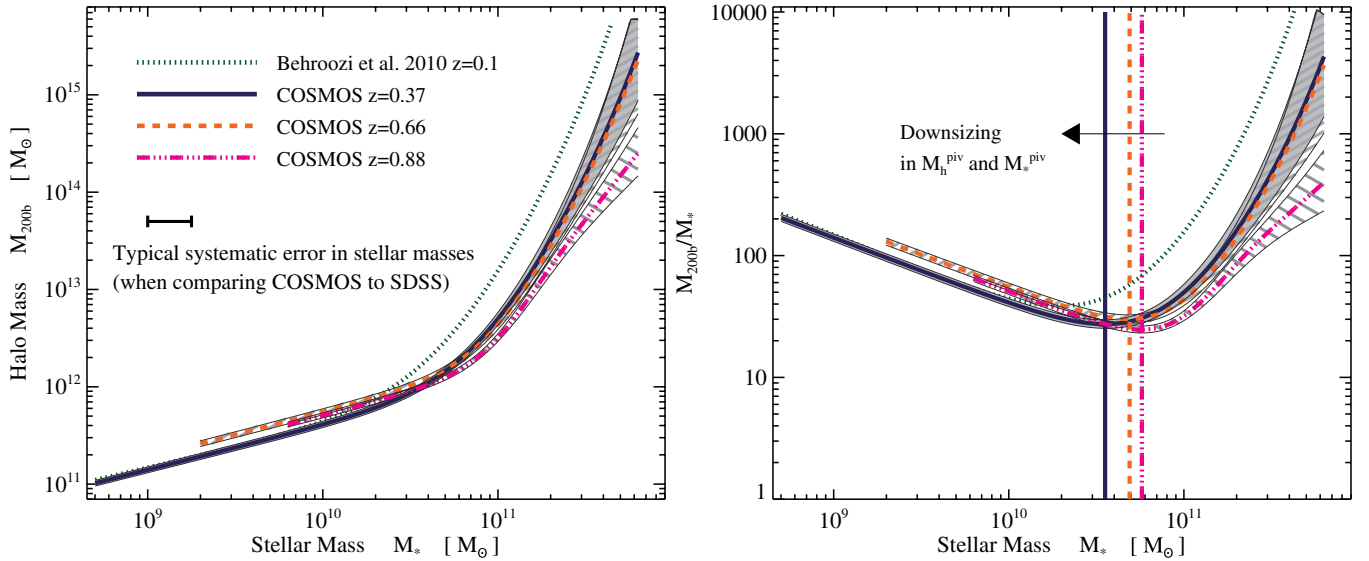
Figure 11. Left panel: redshift evolution in the SHMR. Because the COSMOS results have been derived in a homogeneous fashion, we can inter-compare the three COSMOS redshift bins. The low-mass slope of the SHMR remains constant with $\beta \sim 0.46$. We detect a clear evolution in M_*^{piv} and M_h^{piv} which are respectively the stellar and halo mass at which M_{200b}/M_* reaches a minimum (see the right panel). At high masses, there is an interesting hint that the amplitude of the SHMR is decreasing at higher redshifts, but we lack the statistics to make a clear detection, mainly due to the small volume probed by COSMOS. We have also plotted the SHMR reported by B10. However, caution must be taken when making a direct comparison between COSMOS and B10 because our stellar masses have been derived under different assumptions. According to B10, the level of systematic uncertainty in stellar masses is of order 0.25 dex. Given this 0.25 dex systematic uncertainty, we are in broad agreement with B10 but a direct comparison would require a more homogeneous analysis between COSMOS and SDSS. Right panel: redshift evolution in M_{200b}/M_*. Both M_*^{piv} and M_h^{piv} exhibit downsizing trends, decreasing at later epochs. This effect is shown more explicitly in Figure 12.

(A color version of this figure is available in the online journal.)

converted to M_{200b} assuming a Navarro–Frenk–White (NFW) profile and a Muñoz-Cuartas et al. (2011) mass–concentration relation for a WMAP5 cosmology when necessary. All results quoted here assume either a Kroupa or a Chabrier IMF. Since the systematic shift in M_* between these two IMFs is small (~ 0.05 dex), we do not adjust for this difference. We also do not attempt to correct for differences in the assumed cosmological model.

5.5.1. Comparison with Previous Work: Low Redshift

Mandelbaum et al. (2006a) have used g–g lensing in the SDSS to measure halo masses for lens galaxies at $z \sim 0.1$. Since Mandelbaum et al. (2006a) only present their results as a function of both M_* and color, the data points in Figure 10 have been re-computed as a function of M_* only (Rachel Mandelbaum 2011, private communication). Except perhaps for one data point at low M_*, these results are in good agreement with ours.

At high masses, an alternative method to probe the central SHMR is to directly compare the halo masses of groups and clusters of galaxies to the masses of their central galaxies. Since we are primarily interested in $\Phi_c(M_*|M_h)$, it is critical, as much as possible, to use *halo mass* selected samples of groups and clusters for this type of comparison. Using samples selected on the basis of the stellar mass of the central galaxy, for example, would result in biased conclusions. In Leauthaud et al. (2010), we presented a sample of X-ray groups ($M_{200b} \sim 10^{13}$–$10^{14}\ M_\odot$) in COSMOS for which we have calibrated the relationship between halo mass and X-ray luminosity (L_X) using g–g lensing. The expected scatter in halo mass at fixed L_X is of order 0.13 dex so the sample presented in Leauthaud et al. (2010) is halo mass selected to a good approximation. In parallel, George et al. 2011 and M. R. George et al. (in preparation) have constructed an algorithm to identify the central galaxies

of these groups and have used the weak lensing signal itself to optimize the algorithm by maximizing the weak lensing signal at small radial separations from the central galaxy. The gray squares in Figure 10 report the stellar mass of the central galaxy versus M_h for groups at $0.22 < z < 0.48$ and with a high-quality flag. These data points are directly comparable to ours since we have used exactly the same stellar masses and confirm that our results are consistent with Leauthaud et al. (2010).

We present a similar exercise for a sample of X-ray luminous clusters (A68, A209, A267, A383, A963, A1689, A1763, A2218, A2390, A2219) from Hoekstra (2007) with weak lensing masses from Mahdavi et al. (2008). The central galaxies of these clusters have been studied in detail by Bildfell et al. (2008). Using the same stellar mass code and assumptions as in this paper, we have computed stellar masses for the central cluster galaxies using a compilation of optical data provided by Chris Bildfell. The results are shown by the red asterisk points in Figure 10. Unfortunately, these mass estimates are based on just two optical bands (*B*-band and *R*-band) and as such will have larger uncertainties than the COSMOS stellar masses used in this paper which are constrained with many more filters and normalized to a near-IR luminosity. We estimate that an additional 0.25 dex stellar mass uncertainty should be included when interpreting these data points, which may account for their scatter in stellar mass seen in Figure 10. With this cautionary note, plus the additional caveat that this sample is not as homogeneously selected as the groups from Leauthaud et al. (2010), and that COSMOS is too small to probe overdensities of these masses, the results are nonetheless in good agreement with the extrapolation of our z_1 SHMR.

Both Moster et al. (2010) and B10 have presented constraints on the SHMR and its redshift evolution by using the abundance matching technique. A more detailed comparison with their work is presented in Sections 5.5.3 and 5.5.4.

Conroy et al. (2007) have used the kinematics of satellite galaxies in SDSS and DEEP2 (Davis et al. 2003) to probe the SHMR at $z \sim 0.06$ and at $z \sim 0.8$. Their low-redshift results are shown by the blue diamonds in Figure 10. A 30% downward correction to halo masses has been applied due to incompleteness effects as described in their paper. In addition to systematic differences in stellar mass estimates, direct comparisons with our results are further complicated by the fact that our model describes $\langle \log_{10}(M_*(M_h)) \rangle$ whereas the Conroy et al. (2007) results represent $\langle M_h(M_*) \rangle$. The two averaging systems will yield different results: $\langle M_h(M_*) \rangle$ will be increasingly biased low with respect to $\langle \log_{10}(M_*(M_h)) \rangle$ with increasing $\sigma_{\log M_*}$ and for steeper values of the slope of the SHMR.

More et al. (2010) have used SDSS data to probe the halo masses of ~ 3900 central galaxies in the range $0.02 \leqslant z \leqslant 0.072$ using the kinematics of satellite galaxies. In their paper, More et al. (2010) have analyzed red and blue galaxies separately. For Figure 10 we have asked the authors to provide the data for all central galaxies as a function of M_*, irrespective of color, and also to convert their results to reflect the mean–log relation ($\langle \log_{10}(M_*(M_h)) \rangle$ as opposed to $\langle M_h(M_*) \rangle$). Overall, there is some disagreement between our results and More et al. (2010) regarding the general shape of the SHMR. Indeed, our results display a more strongly varying power-law index compared to More et al. (2010). This disagreement is perhaps more apparent in the lower panel of Figure 10. Indeed, the More et al. (2010) results display a fairly broad minimum in M_{200b}/M_* whereas our results predict a more strongly varying M_{200b}/M_* ratio that reaches a minimum at $M_* \sim 4.5 \times 10^{10} M_\odot$. More et al. (2010) have suggested that satellite kinematics may yield halo masses that may be systematically higher by a factor of two to three than other methods at low M_*. Lowering the More et al. (2010) results at low M_* would certainly bring their results into better agreement with ours in terms of the shape of the SHMR. More et al. (2010) also provide estimates for $\sigma_{\log M_*}$. They find $\sigma_{\log M_*} = 0.19_{-0.03}^{0.03}$ for red centrals and $\sigma_{\log M_*} = 0.15_{-0.07}^{0.12}$ for blue centrals. Both of these values are in broad agreement with our estimate of $\sigma_{\log M_*} \sim 0.23$ dex.

In the z_1 redshift bin, the COSMOS results are limited by completeness to $M_* > 10^{8.7} M_\odot$. Nonetheless, it is of interest to see how our results extrapolate to galaxies of even lower stellar masses, even though measurements of M_h for such low-mass galaxies are fraught with difficulties and for the most part limited to the local volume. Blanton et al. (2008) have presented an effort to address the very low mass SHMR (see their Figure 12) using measurements of the maximum circular velocities from H I disks around isolated nearby dwarf galaxies. Since Blanton et al. (2008) have applied criteria to specifically select isolated galaxies, their sample should be dominated by central galaxies and so comparable to our Figure 10. Upon request, the authors provided us with the full data set from Figure 12 in Blanton et al. (2008) which we have reproduced in Figure 10, including additional data from Springob et al. (2005) and Pizagno et al. (2007) based on H I and Hα rotation curves, respectively. This data compilation is restricted to galaxies that are isolated and with axis ratios $b/a < 0.5$ in order to minimize inclination uncertainties and extinction corrections. Halo masses in Blanton et al. (2008) have been estimated by assuming that the optical circular velocity, $V_{\rm opt}$, is equal to $V_{\rm max}$, the maximum circular velocity for an NFW halo. $V_{\rm max}$ is then converted to the virial velocity, V_{200}, using N-body calibrations from Bullock et al. (2001). For galaxy mass halos, $V_{\rm max}/V_{200} \simeq 1.1$–1.2 under the assumption of no adiabatic contraction of the dark matter due

to galaxy formation. When incorporating adiabatic contraction into Tully–Fisher analyses, Gnedin et al. (2007) find a factor of ~ 2.5 decrease in the inferred halo mass at fixed stellar mass. Such a correction would put the Tully–Fisher constraints into better agreement with our results.

To first order, there is relatively good agreement between our SHMR and the data from Blanton et al. (2008), albeit with a much larger scatter in the Tully–Fisher based SHMR than predicted by our results. In particular, the dwarf galaxy data points from the Geha et al. (2006) sample are in good agreement with the extrapolation of our SHMR to lower masses. At $10^9 M_\odot < M_* < 10^{11} M_\odot$, however, there may be some indication that the halo masses inferred by Blanton et al. (2008) are too high on average compared to our results with the possible implication that the $V_{\rm opt}/V_{200}$ is larger than 1.1–1.2. The $V_{\rm opt}/V_{200}$ ratio contains information about the relative importance of baryons versus dark matter on galaxy scales: $V_{\rm opt}/V_{200} \geqslant 1.1$–1.2 would imply that the baryons have modified the dark matter profile in the very inner halo regions. Dutton et al. (2010) have used the Pizagno et al. (2007) data in combination with a compilation of prior work on the SHMR to place constraints on $V_{\rm opt}/V_{200}$ for late-type galaxies (the requirement that the Pizagno et al. 2007 galaxies have sufficiently extended Hα emission to yield a useful rotation curve implies that this is primarily a late-type sample). They find that $V_{\rm opt} \sim V_{200}$, however, the normalization of the SHMR that they employ is more similar to the More et al. (2010) results than to ours. Therefore, a similar analysis as Dutton et al. (2010) but applied to the Pizagno et al. (2007) data in combination with our results would yield a higher $V_{\rm opt}/V_{200}$.

The agreement between the extrapolation of our SHMR to lower masses and the Geha et al. (2006) sample is encouraging. In fact, Busha et al. (2010) found that a similar scaling continues to work down to the faintest satellites of the Milky Way. However, Figure 10 clearly reveals a lack of data at $M_* < 10^9 M_\odot$ due to the stellar mass completeness limits of current optical and IR surveys. Pushing the SHMR down to $10^8 M_\odot < M_* < 10^9 M_\odot$ using techniques such as described in this paper is clearly an exciting avenue to explore and will be facilitated by upcoming very deep optical and IR surveys such at UltraVista and the Hyper Suprime Cam (HSC) survey on the Subaru telescope.[25]

5.5.2. Comparison with Previous Work: High Redshift

Heymans et al. (2006a) have used g–g lensing to estimate halo masses for a sample of 626 galaxies with $M_* > 10^{10.5} M_\odot$ and with $0.2 < z < 0.8$ from the 0.25 deg^2 *HST*/GEMS (galaxy evolution from morphology and SEDs) survey (Rix et al. 2004). Heymans et al. (2006a) find $M_{\rm vir}/M_* = 53_{-16}^{+13}$ at a mean stellar mass of $M_* = 7.2 \times 10^{10} M_\odot$. Converting their result to our assumed value of H_0 and to M_{200b} yields $M_{200b}/M_* \sim 58_{-17}^{+14}$. In a similar mass and redshift range, our results produce $M_{200b}/M_* \sim 34$. We note, however, that a careful comparison between our work and Heymans et al. (2006a) is limited by several differences in the way the analyses have been performed. First, Heymans et al. (2006a) fit an NFW profile to the g–g lensing signal and so the masses that they measure will reflect the mean halo mass at fixed stellar mass,

---

[25] For example, the UltraVista survey of the COSMOS field will obtain IR imaging to $Y = 26.7$, $J = 26.6$, $H = 26.1$, and $K_s = 25.6$ mag, pushing low-redshift stellar mass completeness limits to below $M_* = 10^8 M_\odot$ at $z < 0.3$. The HSC intermediate layer survey will cover 20 deg^2 to $g = 28.6$, $r = 28.1$, $i = 27.7$, $z = 27.1$, and $Y = 26.6$ mag.

which is different than our averaging system. Second, Heymans et al. (2006a) do not account for the contribution of satellite galaxies to the g–g lensing signal and so they will tend to overestimate halo masses. The lens sample of Heymans et al. (2006a) is roughly similar to our g–g bin4 in the z_2 redshift range: the contribution to the g–g lensing signal from satellites for this sample is shown in panel (j) of Figure 6. Given these two caveats our results are in fairly good agreement.

5.5.3. Comparison with Moster et al.

Moster et al. (2010) derive constraints on the redshift evolution of the SHMR by abundance matching to the SDSS SMF of Panter et al. (2007) at low redshift and to mass functions from the MUNICS survey (detection limit $K \sim 19.5$, area 0.28 deg^2; Drory et al. 2004) and the GOODS-MUSIC sample (detection limit $K \sim 23.5$, area 143.2 arcmin^2; Fontana et al. 2006) at high redshift. There are two main differences between Moster et al. (2010) and our work. First, we adopt the functional form advocated by B10 for the SHMR which is sub-exponential at high M_*. In contrast, the Moster et al. (2010) parameterization asymptotes to a power law at high M_*. According to B10, such a parameterization may be problematic. Indeed, because the logarithmic slope of the SHMR increases with increasing M_*, the best-fit power law for high-mass galaxies will depend on the upper limit in the available data for the SMF. Second, the Moster et al. (2010) errors do not reflect possible systematic errors in stellar mass estimates between Panter et al. (2007), Drory et al. (2004), and Fontana et al. (2006).

Although we find the same qualitative behavior as Moster et al. (2010): M_h/M_* decreases to a minimum at $M_h \sim 10^{12} \, M_\odot$ and then rises at higher masses, interestingly, our results differ regarding the evolutionary trends of the SHMR. The two parameters for which our conclusions differ in particular are $M_*^{\rm piv}$ and $(M_h/M_*)^{\rm piv}$. In Figure 12 (yellow dash-dotted line), we show the evolution of $M_h^{\rm piv}$, $M_*^{\rm piv}$, and $(M_h/M_*)^{\rm piv}$, as inferred from Table 7 in Moster et al. (2010).

Our results agree with Moster et al. (2010) in terms of the qualitative downsizing trend seen for $M_h^{\rm piv}$. However, it is interesting to note that our measurements differ with respect to the normalization of $M_h^{\rm piv}$. The exact origin of this discrepancy remains unclear. In light of the results of B10, we hypothesize that this discrepancy may be caused by the difference in the assumed parametric form of the SHMR. In any case, further investigation regarding the source of this discrepancy, though beyond the scope of this paper, is clearly warranted.

Our conclusions differ with respect to $M_*^{\rm piv}$ and $(M_h/M_*)^{\rm piv}$. Whereas our results suggest that $M_*^{\rm piv}$ increases with redshift and that $(M_h/M_*)^{\rm piv}$ remains constant, in contrast, the Moster et al. (2010) results imply that $M_*^{\rm piv}$ is constant with redshift and that instead, $(M_h/M_*)^{\rm piv}$ increases with redshift. We hypothesize that this discrepancy is simply due to the fact that the errors in Moster et al. (2010) are likely to be underestimated. Indeed, accounting for sample variance with mocks as well as for systematic differences in the relative stellar masses between Panter et al. (2007), Drory et al. (2004), Fontana et al. (2006) would lead to similar errors as B10 (Figure 12, green diamonds). Indeed, the evolution that we detect in $M_*^{\rm piv}$ is $\sim$0.21 dex from $z = 0.37$ to $z = 0.88$ which is similar to the expected error in stellar mass estimates between different surveys. This could perhaps also explain why we reach similar conclusions regarding the evolution of M_h (which should be less affected by systematic errors associated with M_*) but not $M_*^{\rm piv}$ or $(M_h/M_*)^{\rm piv}$.

5.5.4. Comparison with Behroozi et al.

The closest comparison with our work is B10 since we employ the same functional form for the SHMR, the same halo mass function from Tinker et al. (2008), and we both account for the effect of scatter in the SHMR and for sample variance in the data using mock catalogs.

B10 derive constraints on the redshift evolution of the SHMR by abundance matching to the SDSS SMF of Li & White (2009) at low redshift and to mass functions from the FIDEL Legacy Project in the extended Groth strip at higher redshifts (Pérez-González et al. 2008). As a result of the fact that B10 combine data from distinct surveys, their systematic uncertainties on the evolution of the SHMR are fairly large. We also note that there are differences between the stellar mass estimates used in B10 and in this paper (see Section 5.6) which will lead to normalization differences in $M_*^{\rm piv}$ and $(M_h/M_*)^{\rm piv}$ for example.

Another difference between B10 and our work is the treatment of satellite galaxies. In our model, the SHMR only applies to central galaxies and satellites are modeled via $\langle N_{\rm sat} \rangle$. Indeed, we require a more sophisticated treatment of satellites in order to fit the clustering and the g–g lensing for which the satellite term plays a larger role than in the SMF (the satellite term is subdominant at all scales for the SMF). In contrast, B10 assume that the SHMR applies also to satellite galaxies, on condition that the "halo mass" for satellite galaxies is defined as the halo mass at the epoch when satellites were accreted onto their parent halos (the "infall mass," $M_{\rm infall}$). Thus, there could be subtle differences between the two methods due to the treatment of satellite galaxies (for example, see discussion in Neistein et al. 2011).

Figure 12 (green diamonds) shows the prediction from B10 for the pivot quantities. Our results are in striking agreement with B10 with respect to the evolution of $M_h^{\rm piv}$. The errors from B10 are larger for $M_*^{\rm piv}$ and $(M_h/M_*)^{\rm piv}$. Thus our results agree with B10 in terms of qualitative evolutionary trends for $M_*^{\rm piv}$ and $(M_h/M_*)^{\rm piv}$. There is a normalization difference for $M_*^{\rm piv}$ between B10 and our results. However, this normalization offset is not unexpected given systematic differences due to varying assumptions for stellar mass estimates. We address this issue further below.

5.5.5. Testing the Redshift Evolution of the Pivot Masses

Given the striking downsizing signal that we detect for the pivot masses, we would like to check that this result is not an artifact of the method we are using. As such we have also re-analyzed the three COSMOS SMFs using the abundance matching method of B10. In this test, the method followed here is identical to that of B10 but with different constraints on the SMF. Specifically, we use the three cosmos SMFs to constrain the redshift evolution of the SHMR and do not include any SDSS data. The results are shown in Figure 13. We find that the downsizing signal for $M_h^{\rm piv}$ and $M_*^{\rm piv}$ is clearly detected in the COSMOS data using the methods of B10. This provides an independent test on our detected evolution of the pivot quantities and suggests that the detected downsizing signal is robust to the methodology that is employed.

This test also raises the interesting question of how the method used in this paper (an HOD-based model that includes fits to clustering and g–g lensing) compares to the method of B10 (abundance matching using only the SMF). As can be seen in Figure 13, we find that the two methods yield very similar results for the pivot quantities. We do however find subtle differences
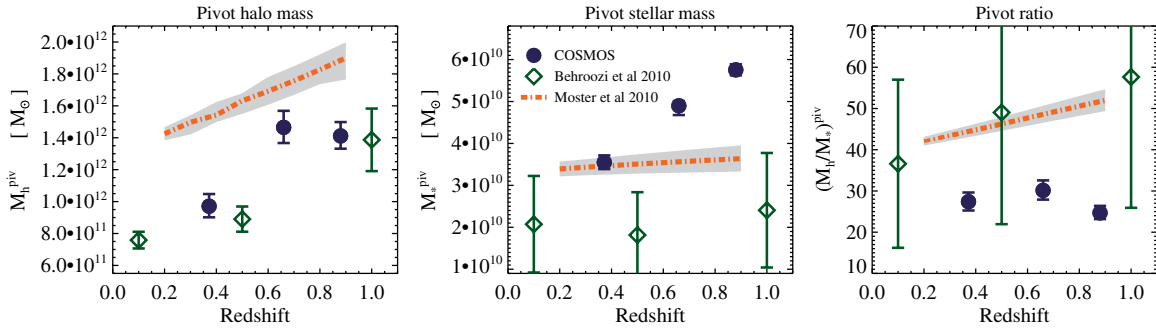
Figure 12. Redshift evolution in the pivot halo mass, the pivot stellar mass, and the pivot ratio. Dark blue circles show the results from this paper. We detect a striking evolution in $M_*^{\rm piv}$ with $M_*^{\rm piv}$ decreasing at later epochs. This downsizing in $M_*^{\rm piv}$ is accompanied by a downsizing in $M_h^{\rm piv}$ with $M_h^{\rm piv}$ also decreasing at later epochs. We detect no strong evolution in the pivot ratio which remains constant at $(M_h/M_*)^{\rm piv} \sim 27$. Green diamonds: comparison with B10. Yellow dash-dotted line: comparison with Moster et al. (2010) (from Table 7 of their paper). The downsizing trend in $M_h^{\rm piv}$ (which is not sensitive to systematic errors associated with M_*) is detected by all three studies. The normalization and evolution of $M_h^{\rm piv}$ is similar for COSMOS and for B10. However, the normalization of $M_h^{\rm piv}$ from Moster et al. (2010) is higher than our prediction. This could be due to differences in the adopted parametric form of the SHMR. The three studies show different results for the evolution of $M_*^{\rm piv}$. We stress that stellar mass estimates computed under different assumptions may present relative systematic errors of order 0.25 dex. This error will affect quantitative comparisons for the normalization $M_*^{\rm piv}$ (and by consequence, also $(M_h/M_*)^{\rm piv}$). Since our results have been derived homogeneously from $z = 0.2$ to $z = 1$, our conclusions regarding the evolutionary trends of $M_*^{\rm piv}$ should be robust. In contrast, B10 and Moster et al. (2010) infer evolutionary trends from a combination of SDSS data and other distinct surveys at higher redshifts. Therefore, their results have larger systematic uncertainties with respect to $M_*^{\rm piv}$. These systematic errors are reflected in the B10 error bars (B10 account for systematic errors and sample variance). The Moster et al. (2010) results do not account for systematic error or sample variance from mock catalogs. Adding these two sources of error to the Moster et al. (2010) results would lead to errors on the pivot quantities of roughly the same order as B10. Given these considerations: both the B10 and the Moster et al. (2010) results (provided larger errors are included) are consistent with our detection of an evolving $M_*^{\rm piv}$ and a constant $(M_h/M_*)^{\rm piv}$.

(A color version of this figure is available in the online journal.)
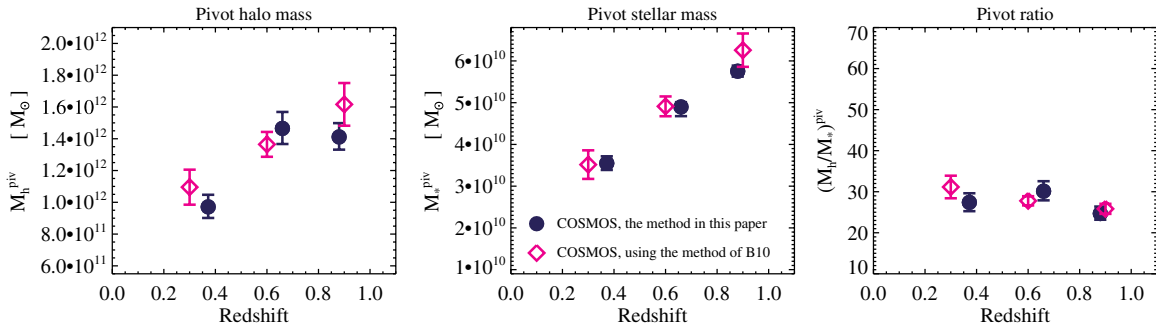

Figure 13. Independent validation of the evolution of the pivot masses using the abundance matching method of B10. Blue circles show our detected evolution of the pivot quantities. Magenta diamonds show the evolution of the pivot quantities when the abundance matching method of B10 is applied to the COSMOS SMFs. We find that the analysis of B10 applied to the COSMOS results fully agrees with our claims concerning the evolution of the pivot quantities. We conclude that the detected downsizing behavior of $M_h^{\rm piv}$ and $M_*^{\rm piv}$ is robust to the methodology that is employed.

(A color version of this figure is available in the online journal.)

in the actual SHMRs between the two methods. Tracking down the cause of the exact differences, although a very interesting question in itself, is beyond the scope of this paper and we defer this study to follow-up work. For the purposes of this paper, we will simply emphasize that the analysis of B10 applied to the COSMOS results fully agrees with our claims concerning the evolution of the pivot quantities.

5.6. The Role of the Stellar Mass Function

In our analysis, the errors on the SMF are small compared to the clustering and the lensing. It is always the case that a measurement of a one-point statistic from a given set of data is more precise than a measurement of a two-point (or higher) statistic. Thus, the SMF plays an important role in constraining our parameter set. Therefore, we investigate the SMF in further detail in this section, and in particular, we show a more in-depth comparison with SDSS mass functions.

Figure 14 shows the COSMOS mass functions compared to various SDSS mass functions that have been commonly employed in the literature (Panter et al. 2007; Baldry et al. 2008;

Li & White 2009). The main difference that we may expect between the COSMOS mass functions and the SDSS ones (besides sample variance and systematic error) is that the high end of the mass function may be inflated due to a larger value of $\sigma_{\log M_*}$ in COSMOS. To gauge how much the COSMOS mass functions are affected by Eddington bias compared to SDSS, we use our model to predict the COSMOS mass functions, deconvolved to the expected scatter for SDSS ($\sigma_{\log M_*} \sim 0.17$ dex). The results are shown in the right-hand panel of Figure 14. We find that the difference in scatter is not significant enough to explain the differences between the COSMOS and SDSS mass functions. It is more likely that the differences are due, for example, to varying assumptions regarding stellar population and dust models.

The difference between COSMOS and Li & White (2009) corresponds roughly "by eye" to a "left/right" shift along the X-axis ($\log_{10}(M_*^{\rm li}) \sim \log_{10}(M_*^{\rm cosmos}) - 0.2$). This difference is within the estimated systematic uncertainties (0.25 dex according to B10). However, this type of systematic shift will be reflected directly in the SHMR (Figures 10 and 11) by a "left/right" shift along the X-axis and will also affect the
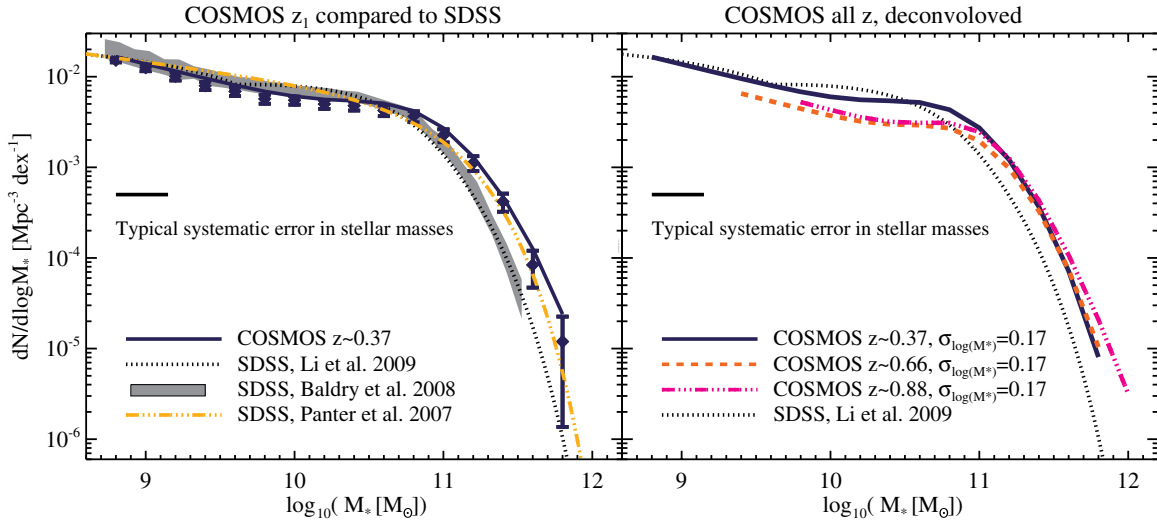
Figure 14. Comparison of the COSMOS stellar mass functions to the SDSS mass functions of Panter et al. (2007), Baldry et al. (2008), and Li & White (2009). In the left panel, we show the COSMOS z_1 mass function. The error bars represent the expected sample variance in COSMOS. In the right panel, we show the mass functions for all three COSMOS mass functions, de-convolved to a common $\sigma_{\log M_*}$ of 0.17 dex. The differences between the COSMOS mass functions and the SDSS mass functions cannot be explained by Eddington bias and are therefore more likely to be due, for example, to differences in assumptions regarding stellar population and/or dust models.

(A color version of this figure is available in the online journal.)
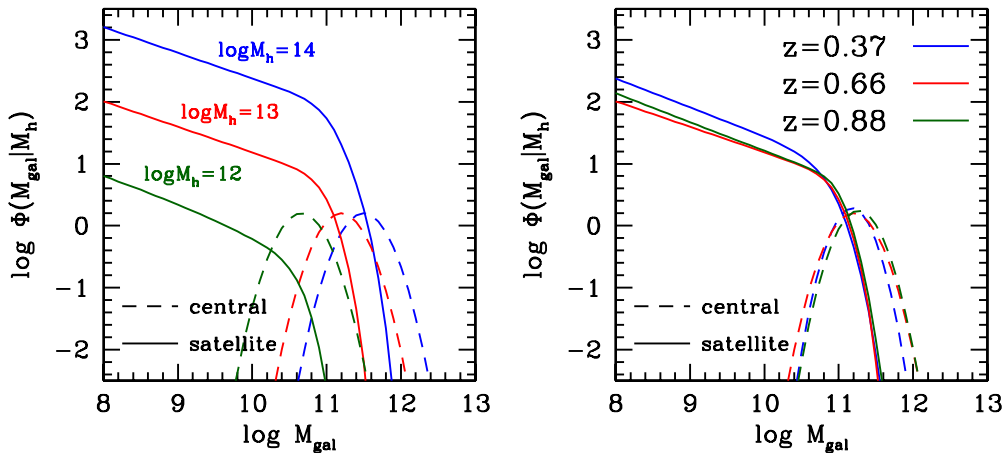
Figure 15. Left panel: the conditional stellar mass functions for central and satellite galaxies for three different halos masses. Results are for $z = 0.66$. Solid curves represent $\Phi_s(M_*|M_h)$ while dashed curves represent $\Phi_c(M_*|M_h)$. The curves are normalized such that the total area is the mean number of galaxies at that halo mass. Right panel: conditional stellar mass functions for halos of $M_h = 10^{13} M_\odot$ for our three redshift bins.

(A color version of this figure is available in the online journal.)

normalization of $M_*^{\rm piv}$ and $(M_h/M_*)^{\rm piv}$. This $\sim$0.2 dex shift would bring the normalization of B10 into closer agreement with our results. Tracking down the exact source of this systematic shift is beyond the scope of this paper but it could be associated with differences in the assumed dust model[26] for example.

We conclude that in order to use the low-z SDSS data as a $z \sim 0$ anchor to study the redshift evolution of the SHMR, a homogeneous analysis of both the SDSS and the COSMOS data is critical. This will be the focus of a future paper.

5.7. The Total Galaxy Stellar Content as a Function of Halo Mass

Figure 15 shows the conditional SMFs for various halo masses and redshifts from our best-fit model. We can use these functions to calculate the *total* amount of stellar material locked up

in galaxies as a function of halo mass, noted hereafter $M_*^{\rm tot}$ (see Equation (16) in Paper I). Investigating $M_*^{\rm tot}$ is of interest because it reveals the efficiency with which dark matter halos accumulate stellar mass from the combined effects of in situ star formation and accretion via merging.

One might worry that calculating the total amount of stellar material locked up in satellite galaxies requires extrapolating our model beyond the lower and upper stellar mass bounds for which our model has been calibrated. As discussed in Section 5.5.1, the extrapolation of our model is in good agreement with results from Blanton et al. (2008) at low M_* and with Hoekstra (2007) at high M_*. Thus, to first order, this extrapolation does not appear unreasonable. Let us therefore make the assumption that the extrapolation of our SHMR is not wildly incorrect. We will now investigate which mass range of satellite galaxies contributes most to $M_*^{\rm tot}$.

From Figure 15, it is clear that satellite galaxies are a sub-dominant component of the total stellar mass at $M_h = 10^{12} M_\odot$.

---

[26] Our stellar masses used the Charlot & Fall (2000) dust model whereas Li & White (2009) use Blanton & Roweis (2007).
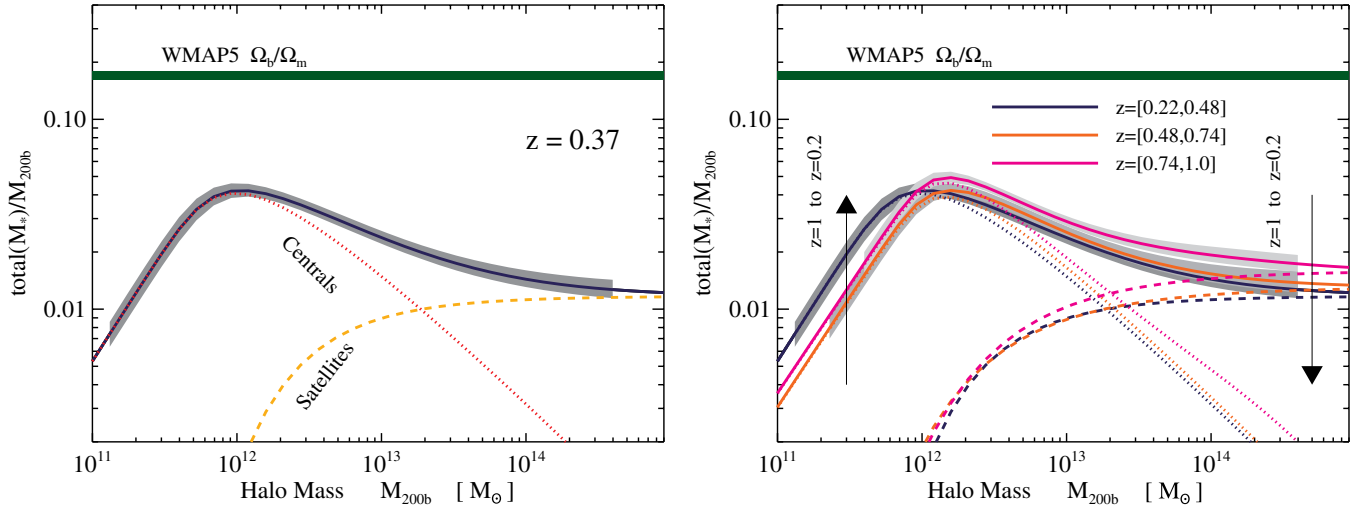
Figure 16. Total stellar content locked up in galaxies as a function of halo mass compared to the cosmic baryon fraction measured by the *Wilkinson Microwave Anisotropy Probe* (WMAP5; $f_b = \frac{\Omega_b}{\Omega_m} = 0.171 \pm 0.009$; Dunkley et al. 2009). Left panel: our prediction from the z_1 bin ($z \sim 0.37$). Right panel: our three redshift bins. z_1 is shown by the solid dark blue line, z_2 is shown by the orange line, and z_3 is shown by the magenta line. Dotted lines show the contribution to $M_*^{\rm tot}$ from the central galaxy and dashed lines show the contribution from satellite galaxies. Shaded regions represent the errors on $M_*^{\rm tot}/M_{200b}$. $M_*^{\rm tot}$ is dominated by the central galaxy at $M_h < 2 \times 10^{13}\,M_\odot$ and by satellites at $M_h > 2 \times 10^{13}\,M_\odot$.

(A color version of this figure is available in the online journal.)

Our present concern is therefore only relevant for $M_h > 10^{12}\,M_\odot$. Let us consider the total stellar mass associated with satellite galaxies as a function of M_h in a fixed stellar mass bin: $M_*^{\rm tot,sat}(M_h|M_*^{t1}, M_*^{t2})$. As shown in Paper I, the expression for $M_*^{\rm tot,sat}(M_h|M_*^{t1}, M_*^{t2})$ is given by

$$M_*^{\rm tot,sat}(M_h|M_*^{t1}, M_*^{t2}) = \int_{M_*^{t1}}^{M_*^{t2}} \Phi_s(M_*|M_h) M_* dM_*. \quad (20)$$

We have tested how $M_*^{\rm tot,sat}(M_h|M_*^{t1}, M_*^{t2})$ varies with the integral limits, M_*^{t1} and M_*^{t2}. We find that at fixed halo mass, most of the stellar mass associated with satellite galaxies arises from a relatively narrow range in stellar mass. In particular, for halos with $M_h > 10^{11}\,M_\odot$, the bulk of $M_*^{\rm tot,sat}$ is built from satellite galaxies in the range $10^{10}\,M_\odot < M_* < 10^{11}\,M_\odot$. Therefore, provided that the extrapolation of our model is not wildly incorrect, the bulk of $M_*^{\rm tot,sat}$ arises from satellites that are within the tested limits of our model.

Having underlined this caveat, we have calculated $M_*^{\rm tot}$ using the best-fit parameters for each of the three redshift bins and the results are shown in Figure 16. This figure will be discussed in detail in the following section.

6. DISCUSSION

Using a self-consistent framework to simultaneously fit the g–g lensing, spatial clustering, and number densities of galaxies in COSMOS, we have obtained a robust characterization of the evolving relationship between stellar mass and halo mass over two orders of magnitude in M_*. The nature of this relationship, shown in Figure 16, is not only a byproduct of cosmic mass assembly but is also shaped by the physical processes that drive galaxy formation, ultimately providing valuable constraints on both. In this section, we begin by discussing various processes that shape the form of M_*/M_h versus M_h. We will then introduce a simple framework for interpreting evolution in this relation by considering the relative growth of stellar mass as compared to the growth of dark matter halos. Finally, we will discuss the

observed evolution of the pivot quantities and we will show how a constant pivot ratio may imply that the mechanism responsible for the shutdown of star formation in massive galaxies may have a physical dependence on M_*/M_h.

6.1. The Total Stellar Mass Content of Dark Matter Halos

Figure 16 separates the stellar content of the average dark matter halo into a contribution from the central galaxy and a contribution from the sum of satellite galaxies. Central galaxies show an M_*/M_h ratio that rises steeply to a maximum at $M_h \sim 10^{12}\,M_\odot$ before decreasing somewhat more gradually in halos of higher mass. The fact that halos above this mass scale (at the redshifts considered) have cooling times longer than their dynamical times has been invoked by modelers for some time to help explain why cooling and star formation shut down at the highest masses, with some refinement due to the presence of so-called cold-mode accretion (Birnboim & Dekel 2003; Kereš et al. 2005; Birnboim et al. 2007; Cattaneo et al. 2006). We will return to the evolution of this mass scale at a later point in the discussion.

Central galaxies strongly dominate the total stellar mass content at $M_h \lesssim 2 \times 10^{13}\,M_\odot$ ("the central dominated regime"), including at the peak mass, $M_h \sim 10^{12}\,M_\odot$, while the stellar mass in satellites dominates at $M_h \gtrsim 2 \times 10^{13}\,M_\odot$ ("the satellite dominated regime").

The transition between the two regimes is driven by the steep decline in $M_*^{\rm cen}/M_h$ at $M_h > 10^{12}\,M_\odot$. This decline occurs as the contribution from satellites begins to rise. One might then naturally ask if central galaxies in group-scale halos experience stunted growth simply because stellar mass is accumulating within the halo in the form of satellite galaxies, instead of merging onto the central galaxy. Figure 16 reveals that this is not the case. Indeed, the solid line in this figure demonstrates that *the total stellar mass fraction of halos declines at $M_h > 10^{12}\,M_\odot$*. Thus, even if all satellite galaxies were allowed to rapidly coalesce at the center of the potential well, the central galaxies of group-scale halos would still have lower M_*/M_h ratios than those in halos of $M_h \sim 10^{12}\,M_\odot$. Thus, we conclude that dark

matter halos globally decline in the efficiency by which they accumulate stellar mass at $M_h > 10^{12} M_\odot$.

We note that in massive halos, the intra-cluster light (ICL; not accounted for in this analysis) is estimated to contribute an additional 20%–30% of the total stellar mass (Feldmeier et al. 2004; Zibetti et al. 2005; Gonzalez et al. 2005; Krick et al. 2006). Adding this to the satellite component in Figure 16 does little to bridge the factor of two to four gap in $M_*^{\rm tot}/M_h$ between the satellite component in high-mass halos and centrals at the peak mass.

6.2. The Role of Galaxy Mergers in Determining the Shape of $M_*^{\rm tot}/M_h$

The majority of the total mass in an average dark matter halo is built from halo–halo mergers with mass ratios above 1:10 (e.g., Hopkins et al. 2010a). At halo masses below $10^{12} M_\odot$, the steep rise in $M_*^{\rm tot}/M_h$ with M_h implies that the typical *stellar* mass ratio of galaxy mergers will be less than the typical mass ratio of the dark matter halos hosting these galaxies. In other words, *major halo mergers are minor galaxy mergers in this regime*. Thus, the accumulation of stellar mass through the effects of merging will be limited compared to the growth in total mass of such halos. The steep rise of $M_*^{\rm tot}/M_h$ must therefore reflect the greater importance of star formation at masses below $M_h \sim 10^{12} M_\odot$ over assembly from galaxy mergers (Bundy et al. 2009). Similar conclusions have also been reached by Conroy & Wechsler (2009) (see their Figures 2 and 3 in particular).

Simple arguments suggest, however, that once halos grow past the pivot mass and in the absence of significant star formation, $M_*^{\rm tot}/M_h$ should dip below the peak value since these halos can only grow by merging with halos with lower values of $M_*^{\rm tot}/M_h$. At slightly higher mass, the decline in $M_*^{\rm tot}/M_h$ now means that stellar mass ratios are enhanced with respect to halo mass ratios, and the trend must reverse again. This repeating pattern should cause a flattening of $M_*^{\rm tot}/M_h$ above the pivot mass. While this behavior is certainly apparent in Figure 16, our different redshift bins also reveal that at fixed mass among high-mass halos ($M_h > 4 \times 10^{13}$), the total stellar mass content *declines* at later epochs. We speculate that this trend could arise from the smooth accretion of dark matter, which brings no new stellar mass, and amounts to as much as 40% of the growth of dark matter halos (e.g., Fakhouri & Ma 2010). One way to test this hypothesis would be to populate a $z = 0.88$ N-body simulation with our z_3 HOD and evolve the subhalo and halo populations to $z = 0$, assuming no star formation. This would reveal the amount of stars that are acquired through mergers in this redshift range (Zentner et al. 2005). We note that the destruction of satellites and a growing ICL component could also contribute to this trend given that the ICL at $z = 0$ could make up 20%–30% of the stellar content of massive halos, roughly the amount by which $M_*^{\rm tot}/M_h$ declines over our redshift range.

6.3. The Pivot Quantities and the Quenching of Star Formation in Central Galaxies

The location at which halos reach their maximum accumulated stellar mass efficiency is encoded by the pivot mass quantities, $M_*^{\rm piv}$, $M_h^{\rm piv}$, and $(M_h/M_*)^{\rm piv}$. While we observe downsizing trends for both $M_*^{\rm piv}$ and $M_h^{\rm piv}$, the co-evolution of these two parameters leaves $(M_h/M_*)^{\rm piv}$ constant with redshift. This can be seen in the right panel of Figure 16: the pivot ratio evolves very little over our redshift range, while the mass scale of the peak
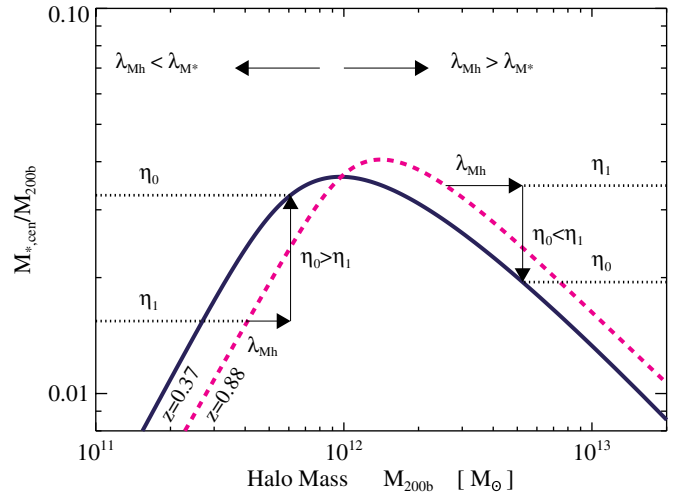

Figure 17. Schematic illustration of our results in terms of galaxy mass assembly vs. halo growth. The magenta line represents our z_3 result and the dark blue line represents our z_1 result. From the relative positions of these two curves we can infer that from $z \sim 0.88$ to $z \sim 0.37$ and at $M_h < 10^{12} M_\odot$, the stellar mass of the central galaxy has experienced a stronger growth in proportion to the growth of the dark matter. On the contrary, at $M_h > 10^{12} M_\odot$, the stellar mass of the central galaxy has experienced a more mild growth in proportion to the dark matter.

(A color version of this figure is available in the online journal.)

($M_h^{\rm piv}$) does evolve downward by nearly a factor of two. Given the low satellite content of halos at these masses, merging is not likely to play a dominant role in driving growth in M_* below the pivot peak, arguing instead that the regulation of star formation is key to understanding this behavior. The physical process that sets the pivot peak at $M_h = 10^{12} M_\odot$, and drives the subsequent decline in $M_*^{\rm cen}/M_h$ at higher halo masses, must be linked to the shutdown of star formation in central galaxies. In the reminder of this discussion, we will focus on interpreting the downsizing behavior of the pivot quantities in this context.

6.4. A Simple Model for Interpreting Evolution in M_*/M_h versus M_h

A complete and comprehensive interpretation of our results requires modeling and accounting for dark matter accretion histories, galaxy merger rates, and star formation rates (SFRs) as a function of redshift (for example, see Conroy & Wechsler 2009). Nonetheless, we will introduce some toy models based on simple arguments to provide a first interpretation of our results. Our goal here is to evaluate our results in the context of other observations and theoretical work on galaxy formation models and to set the stage for a more detailed treatment in subsequent work. We begin with a general treatment of evolution in the SHMR and then will focus on applying this treatment to interpret the evolution we observe in the pivot quantities.

The physical basis for evolution in M_*/M_h versus M_h must be considered carefully because the stellar mass and associated halo mass of a galaxy can evolve independently, depending on the mass scale involved and on processes including merging, smooth (diffuse) dark matter accretion, star formation, and even tidal stripping. The sum of these processes on the growth of M_h and M_* shapes the behavior of M_*/M_h versus M_h in different ways, as illustrated by the schematic diagram in Figure 17. Here we let η_1 represent the ratio M_*/M_h at redshift $z_{\rm high}$ and η_0 represent the equivalent ratio at redshift $z_{\rm low}$ with $z_{\rm high} > z_{\rm low}$. We further consider a dark matter halo of mass M_h that has

grown by a relative factor of λ_{M_h} from z_{high} to z_{low}. We can write that $M_h(z_{\text{low}}) = \lambda_{M_h} \times M_h(z_{\text{high}})$. Characterizing growth in the stellar mass of the central galaxy (although similar arguments apply to M_*^{tot}) by a factor of λ_{M_*}, we can simply write that

$$\lambda_{M_*} = \frac{\eta_0}{\eta_1} \times \lambda_{M_h}. \qquad (21)$$

If $\eta_0 > \eta_1$, we infer that $\lambda_{M_*} > \lambda_{M_h}$ and that the stellar mass has experienced a stronger relative amount of growth compared to that of the dark matter from z_{high} to z_{low}. If on the contrary, $\eta_0 < \eta_1$ then the relative growth of the stellar mass is less than the dark matter. Note that this schematic view demonstrates that identical curves for M_*/M_h versus M_h at different redshifts do not necessarily indicate a lack of evolution, since λ_{M_h} is always greater than zero.

We now apply this intuitive framework to the evolution observed in Figure 16. Considering values of η_1 and η_0 applied to the total stellar mass curves in Figure 16, we see that below $M_h = 10^{12}$, the fractional growth in stellar mass outweighs the growth in halo mass. This reflects the greater importance of star formation at low masses over assembly from galaxy mergers, the same conclusion reached above by simply considering the shape of the SHMR. This evolutionary trend reverses above $M_h = 10^{12} \, M_\odot$, consistent with the notion that star formation is largely shut down in centrals above this mass.

6.5. Understanding the Evolution of the Pivot Quantities

We now apply these simple arguments to the evolution in the pivot quantities. We focus only on central galaxies, neglecting the minor contribution from satellites near the pivot mass. The aim here is to explore several simple models for the quenching of star formation and to investigate which models might reproduce the observed evolution of the pivot quantities, namely, a pivot halo and stellar mass that decrease at later epochs (downsizing) but leave the pivot ratio constant.

Shown schematically in Figure 18, we consider how our high-redshift ($z = 0.88$) SHMR relation would evolve toward lower redshifts under several prescriptions for stellar and halo growth. We begin with no assumptions about the SFR but adopt a halo growth rate (λ_{M_h}) that is roughly constant over the mass range spanned by the peak. This assumption is well justified by dark matter mass accretion rates derived from N-body simulations (Wechsler et al. 2002; McBride et al. 2009; Fakhouri et al. 2010). For example, Fakhouri et al. (2010) find that $\dot{M}_h/M_h$ is only weakly dependent on halo mass with $\dot{M}_h/M_h \propto M_h^{0.1}$.

We now consider several different quenching models and investigate their impact on the redshift evolution of the pivot quantities.

1. *No quenching model*. To begin with, we consider a model with no quenching of star formation and in which the stellar growth rate (λ_{M_*}) is constant over the halo mass range spanned by the peak (Row A in Figure 18). We consider the redshift evolution of the SHMR for three values of λ_{M_*} defined with respect to λ_{M_h}. In all three cases, this model leads to an increase in M_h^{piv} with time (contrary to what we observe). We can therefore conclude that λ_{M_*} must vary with M_h, not a surprise given the expectation that the SFR shuts down above $M_h = 10^{12} M_\odot$.

2. *Fixed halo mass for quenching*. We next consider a model in Row B in which star formation is quenched as galaxies cross above a fixed halo mass, M_q. However, this instantaneous quenching model fails to reproduce (not surprisingly) the

downward evolution of M_h^{piv} and also yields evolution in the pivot ratio, which is not detected.

3. *Redshift-dependent halo mass for quenching*. Row C shows a model in which M_q shifts downward with time. This model leads to downsizing in the pivot halo mass if $\lambda_{M_*} > \lambda_{M_h}$ below M_q (Row C, middle panel). However, in order to keep the pivot ratio fixed in this scenario, the growth rate, λ_{M_*}, must be tuned with respect to the rate at which M_q declines. This would require a fortuitous coincidence, but obviously cannot be dismissed as an explanation.

4. *Critical M_*/M_h ratio for quenching*. We finally consider an alternative scenario in which star formation is limited by a critical mass ratio, $\eta_{\text{crit}} \equiv M_*/M_h \approx 0.04$ (Row E). In this model, we can qualitatively reproduce our main results, including the downsizing trends in the pivot stellar and halo mass, and, by construction, a constant pivot ratio set by η_{crit} (compare the middle panel of Row D to the middle panel of Row E). However, in order to produce downsizing behavior in this model, λ_{M_*} must be larger than λ_{M_h} below η_{crit}. It is important to note that if $\lambda_{M_*} \leqslant \lambda_{M_h}$ below η_{crit}, this model would fail to produce downsizing.

The model explored in Row E seems a promising and simple mechanism that can explain the observed evolution of the pivot quantities. We now test if observations are consistent with the requirement that $\lambda_{M_*} > \lambda_{M_h}$ below $M_h \sim 10^{12} \, M_\odot$. A halo of mass $M_h \sim 2 \times 10^{11} \, M_\odot$ grows by a factor of $\lambda_{M_h} \sim 1.4$ from $z = 0.88$ to $z = 0.37$ (Fakhouri et al. 2010). SFRs as a function of M_* and redshift have recently been measured by Noeske et al. (2007), Cowie & Barger (2008), and Gilbank et al. (2010). These measurements indicate that galaxies of mass $M_* \sim 10^{10} \, M_\odot$ grow by roughly a factor of $\lambda_{M_*} = 2$–3 from $z = 0.88$ to $z = 0.37$. Therefore, at $z < 1$ and for $M_h < M_h^{\text{piv}}$, current estimates for halo growth coupled with estimates for stellar growth are indeed consistent with our observation that stellar mass has experienced a stronger relative amount of growth compared to that of the dark matter ($\lambda_{M_h} < \lambda_{M_*}$ below η_{crit}).

We further note that the relatively weak dependence of λ_{M_*} on M_h required to maintain a constant slope in M_*/M_h versus M_h with redshift (again for $M_h < M_h^{\text{piv}}$) is implied by the weak SSFR–M_* relation observed for galaxies with $M_* < M_h^{\text{piv}}$ (a typical power-law fit gives SSFR $\sim M_*^{0.4}$). This could explain why β (the low-mass slope of the SHMR) is observed to remain remarkably constant at $\beta = 0.46$ at $z < 1$.

Given the simple arguments outlined above, we argue that the fact that the pivot ratio remains constant may suggest that *star formation is fundamentally limited by a critical mass ratio*, $\eta_{\text{crit}} \equiv M_*/M_h \approx 0.04$. A very elegant and compelling consequence of this model is that the observed downsizing trends in M_*^{piv} and M_h^{piv} can be automatically explained given the observation that $\lambda_{M_*} > \lambda_{M_h}$ below $M_h \sim 10^{12} \, M_\odot$. Previous work by Bundy et al. (2006) on the evolution of the galaxy SMF has found a similar downsizing trend for the "transition mass," M_{tr}, which is defined in terms of M_* by the declining fraction of star-forming galaxies at the highest masses. The transition mass from Bundy et al. (2006) evolves from $M_{\text{tr}} \sim 9 \times 10^{10} M_\odot$ at $z \sim 0.9$ to $M_{\text{tr}} \sim 5 \times 10^{10} M_\odot$ at $z \sim 0.6$. This transition mass is similar to M_*^{piv}, reinforcing the notion that the pivot mass marks the end of rapid star formation among halos. The obvious difference between Bundy et al. (2006) and this paper is that our work adds a key missing ingredient, which is the evolution of the pivot halo mass and the pivot ratio. If the quenching of star formation depends on a critical M_*/M_h ratio then the fact that
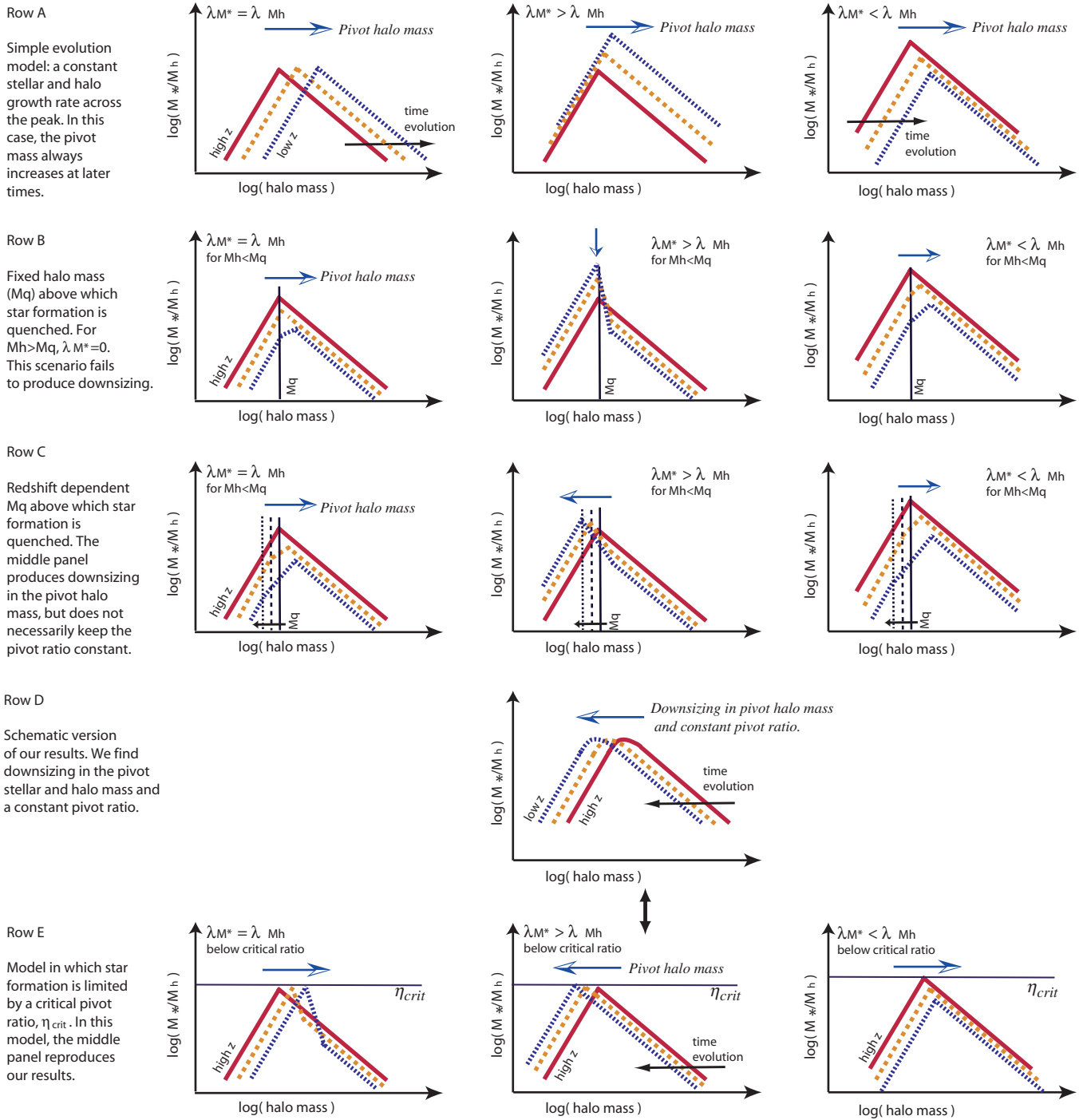
Figure 18. Schematic (and simplistic picture) of how M_*/M_h (for central galaxies) varies with redshift for different quenching models and for various prescriptions for stellar growth and halo growth (parameterized here by λ_{M_*} and λ_{M_h}, respectively). Our z_3 ($z = 0.88$) relation is represented by the solid red line. In this picture, we are not interested in understanding why the high-redshift relation has the particular form that is observed, but simply in predicting roughly what the evolution of this relation should look like given various quenching models. The orange dashed line and the blue dotted line show how we expect the SHMR to evolve with time. In Row A we consider a model without any quenching and where λ_{M_*} and λ_{M_h} are constant with redshift and halo mass. In this model, the pivot halo mass will increase at later epochs which is not what we observe. In Row B, we consider a model in which star formation is quenched above a fixed halo mass, M_q. This model fails to produce the observed downsizing behavior for $M_h^{\rm piv}$. In Row C, we consider a model where M_q decreases at lower redshifts. In this case when $\lambda_{M_*} > \lambda_{M_h}$ below M_q (Row C, middle panel), $M_h^{\rm piv}$ follows a downsizing trend. However, in this scenario, a pivot ratio that is constant with redshift requires a fine tuning between λ_{M_*} and the rate at which M_q declines. In Row E, instead of assuming that star formation is quenched at a fixed halo mass, we now assume that star formation is quenched at a fixed critical M_*/M_h ratio ($\eta_{\rm crit}$). Given this assumption and if $\lambda_{M_*} > \lambda_{M_h}$ below $\eta_{\rm crit}$ (a reasonable assumption given estimates for halo growth and star formation at these scales), we can qualitatively reproduce our main results (compare the middle panel of Row D to the middle panel of Row E).

(A color version of this figure is available in the online journal.)

low-mass galaxies grow more rapidly than dark matter below the pivot scale provides a *simple explanation for the observed downsizing in the sites of star formation* observed by studies such as Bundy et al. (2006).

6.6. Physical Mechanisms that might Depend on M_*/M_h

In the previous section, we demonstrated that a constant pivot ratio provides important clues concerning the physical mechanisms that quench star formation. We now discuss possible mechanisms that might tie quenching to M_*/M_h.

The notion of a fixed maximum stellar-to-dark matter ratio, $\eta_{\rm crit}$, has been relatively unexplored in the literature. Theoretical arguments tend to favor a relatively fixed (if broad) critical halo mass (see Birnboim & Dekel 2003) at $z \lesssim 1$, with significant modifications from cold-mode accretion occurring mostly at higher redshifts. But, quenching at fixed halo mass alone is not sufficient to reproduce the local SMF and red-sequence fraction, and also fails from simple arguments to produce downsizing in the pivot masses, as shown by Row B of Figure 18. As a result, most semi-analytic models include a quenching channel initiated by mergers or disk instabilities among galaxies in halos below the critical halo mass threshold (e.g., Bower et al. 2006; Croton et al. 2006; Cattaneo et al. 2006). Above the critical halo mass, once a quasi-static halo of hot gas has formed, low-luminosity feedback (i.e., radio-mode AGN feedback) is often invoked to prevent cooling and star formation in massive halos at late times. Using simple arguments, we have shown that mergers do not provide a likely explanation for determining the scale of the pivot mass. We therefore focus on AGN feedback and disk instabilities as possible mechanisms.

It is common practice to consider low-luminosity AGN feedback only in halos above a fixed halo mass. However, in practice, efficient AGN feedback is more complex and requires at least two ingredients. First, a quasi-static halo of hot gas must exist to which the AGN jets can couple. However, AGN feedback also requires a sufficiently large black hole to produce jets powerful enough to initiate this coupling. Given that gas cooling rates scale roughly with halo mass and that black hole mass scales roughly with galaxy mass, via the M_*–σ relation (Gebhardt et al. 2000; Ferrarese & Merritt 2000), it is reasonable to speculate that AGN feedback efficiency would depend on M_*/M_h.

Considering the galaxy population broadly, this scenario requires a sufficiently large bulge component for AGN quenching to be effective. While bulges may be built stochastically in galaxy mergers, a further link may tie secular bulge formation via disk instabilities to the value of M_*/M_h, thereby cementing the relationship between quenching and $\eta_{\rm crit}$. It has been shown that disks become unstable to bar modes if the disk mass dominates the gravitational potential (Efstathiou et al. 1982; Mo et al. 1998). Semi-analytic models typically consider that disk instabilities occur if

$$V_{\rm max}/(G_N M_{\rm disk}/r_{\rm disk})^{0.5} \leqslant 1, \qquad (22)$$

where $M_{\rm disk}$ represents disk mass, $r_{\rm disk}$ is the disk radius, and $V_{\rm max}$ is the maximum of the rotation curve. Depending on the implementation of this criterion, $V_{\rm max}$ may be equated either to the halo virial velocity or the disk velocity at its half-mass radius (see discussion in Parry et al. 2009). An instability will cause either a partial or a total collapse of the disk, leading to a burst of star formation at the center, the formation of a spheroid, and also possibly fueling the central black hole. The disk instability

criterion in Equation (22) shows a dependence on $(M_h/M_{\rm disk})$ (relating $V_{\rm max}$ to M_h) which could be reflected in M_h/M_* as the instability converts cold gas into stars. Disk instabilities might therefore play a role in setting the pivot masses and enforcing $\eta_{\rm crit}$. The coincident fueling of the central black hole during the instability may help initiate AGN quenching and regulate the global decline in $M_*^{\rm cen}/M_h$ beyond the pivot mass.

Assuming the disk instability framework, we can test whether the predicted sizes of stable galactic disks given our critical pivot ratio, $\eta_{\rm crit} \equiv M_*/M_h \approx 0.04$, are consistent with observations. Approximating the halo virial velocity for $V_{\rm max}$, we rewrite Equation (22) to derive the maximum size of stable disks:

$$r_{\rm disk} < R_h \times (M_*/M_h). \qquad (23)$$

Applying this criterion to the pivot masses yields the condition that $r_{\rm disk} < 8$ kpc. Interestingly, this condition is very well satisfied by the observed size distributions of disk galaxies which tend to fall off rapidly just below $r_{\rm disk} = 8$ kpc at both $z \sim 0$ (see Figure 11 in Shen et al. 2003) and at $z > 0$ (see Figure 10 in Sargent et al. 2007). We conclude that, via the growth of bulges and initialization of AGN feedback, disk instabilities provide a promising link between our observed critical pivot ratio and quenching, although further investigation is clearly needed.

Finally, we note that $\eta_{\rm crit}$ might also be related to the competition between the cooling and accretion of cold gas in central starbursts and the resulting feedback from either star formation itself or a co-evolving quasar-mode AGN. This Eddington-like limit has been explored in the context of stellar systems by Hopkins et al. (2010b) who derive a maximum stellar surface density from simple arguments. In the context of dark matter halos explored here, similar arguments might naturally yield a fixed value for $\eta_{\rm crit}$ similar to that obtained by our analysis.

7. CONCLUSIONS

The aim of this paper is to study the form and evolution of the SHMR from $z = 0.2$ to $z = 1.0$. To achieve this goal, we have performed a joint analysis of galaxy–galaxy lensing, spatial clustering, and number densities of galaxies in COSMOS. As a result, we have obtained a robust characterization of the evolving relationship between stellar mass and halo mass over two to three orders of magnitude in M_*. The nature of this relationship is not only a byproduct of cosmic mass assembly but is also shaped by the physical processes that drive galaxy formation, ultimately providing valuable constraints on both. A complete and comprehensive interpretation of our results requires modeling and accounting for dark matter accretion histories, galaxy merger rates, and SFRs as a function of redshift. This will be the focus of future work. Nonetheless, we show how simple evolutionary models can already provide a first interpretation of our results, setting the stage for a more detailed treatment in future work. Using simple arguments, we evaluate our results in the context of other observations and theoretical work on galaxy formation models.

We have defined the pivot quantities ($M_*^{\rm piv}$, $M_h^{\rm piv}$, and $(M_h/M_*)^{\rm piv}$) as the location at which halos reach their maximum accumulated stellar mass efficiency. The evolution of the pivot quantities contains key clues about the physical processes that are responsible for the quenching of star formation in halos above $M_h > 10^{12} M_\odot$. While we observe downsizing trends for both $M_*^{\rm piv}$ and $M_h^{\rm piv}$, the co-evolution of these two parameters leaves $(M_h/M_*)^{\rm piv}$ roughly constant with redshift. We argue that

this result raises the intriguing possibility that the quenching of star formation may have a physical dependence on M_h/M_* and not simply on M_h as is commonly assumed. If the quenching of star formation indeed depends on a critical M_*/M_h ratio then the fact that low-mass galaxies grow more rapidly than dark matter below the pivot scale provides a *simple explanation for observations of downsizing in the sites of star formation*. Additional and more precise measurements of the pivot quantities would be highly interesting in order to confirm whether or not the pivot ratio remains constant, or if instead it evolves mildly with redshift. Interestingly, there are hints from the results of Behroozi et al. (2010) that the pivot mass might in fact remain constant back to $z = 4$.

We highlight four avenues of exploration that would be interesting to pursue in the future and that would improve this analysis. First, we note that the comparison of our results with SDSS abundance matching results (e.g., Behroozi et al. 2010) is limited by systematic differences between stellar mass estimates. In order to use the SDSS data set as a low-z anchor point, a homogeneous analysis of SDSS and COSMOS would be necessary. Second, our work in COSMOS is limited at the high-mass end by sample variance. Larger data sets at higher redshifts than SDSS such as the Baryon Oscillation Spectroscopic Survey (BOSS)[27] and the Canada–France–Hawaii Telescope Legacy Survey (CFHTLS)[28] should provide interesting constraints on the evolution of the high-mass end of the SHMR. Third, pushing the SHMR down to $10^8 \, M_\odot < M_* < 10^9 \, M_\odot$ using techniques such as described in this paper is clearly an exciting avenue to explore and will be facilitated by upcoming very deep optical and IR surveys such at UltraVista and the HSC survey on the Subaru telescope. Finally, we note that the SMF is a powerful tool for placing constraints on the SHMR. However, the derivation of SMFs is clearly currently limited by systematic uncertainties in stellar mass estimates. Working toward an improved understanding of stellar mass estimates and toward reducing systematic errors in the SMF will be the single most important avenue for improving the type of analysis presented in this paper.

Finally, while our analysis demonstrates that the combination of multiple and complementary dark matter probes is a powerful tool with which to elucidate the galaxy–dark matter connection, we emphasize that such probe combinations also hold great potential to constrain fundamental physics, including the cosmological model and the nature of gravity. Exploring the sensitivity of the combination of g–g lensing, clustering, and the SMF to cosmological parameters will be the focus of a follow-up paper.

REFERENCES

Agertz, O., Teyssier, R., & Moore, B. 2011, MNRAS, 410, 1391
Baldry, I. K., Glazebrook, K., & Driver, S. P. 2008, MNRAS, 388, 945
Becker, M. R., McKay, T. A., Koester, B., et al. 2007, ApJ, 669, 905
Behroozi, P. S., Conroy, C., & Wechsler, R. H. 2010, ApJ, 717, 379
Berlind, A. A., & Weinberg, D. H. 2002, ApJ, 575, 587
Bernstein, G. M. 2010, MNRAS, 406, 2793
Bildfell, C., Hoekstra, H., Babul, A., & Mahdavi, A. 2008, MNRAS, 389, 1637
Birnboim, Y., & Dekel, A. 2003, MNRAS, 345, 349
Birnboim, Y., Dekel, A., & Neistein, E. 2007, MNRAS, 380, 339
Blanton, M. R., Geha, M., & West, A. A. 2008, ApJ, 682, 861
Blanton, M. R., & Roweis, S. 2007, AJ, 133, 734
Bower, R. G., Benson, A. J., Malbon, R., et al. 2006, MNRAS, 370, 645
Brainerd, T. G., Blandford, R. D., & Smail, I. 1996, ApJ, 466, 623
Brainerd, T. G., & Specian, M. A. 2003, ApJ, 593, L7
Brinchmann, J., & Ellis, R. S. 2000, ApJ, 536, L77
Brooks, A. M., Governato, F., Quinn, T., Brook, C. B., & Wadsley, J. 2009, ApJ, 694, 396
Brown, M. J. I., Zheng, Z., White, M., et al. 2008, ApJ, 682, 937
Bruzual, G., & Charlot, S. 2003, MNRAS, 344, 1000
Bullock, J. S., Kolatt, T. S., Sigad, Y., et al. 2001, MNRAS, 321, 559
Bullock, J. S., Wechsler, R. H., & Somerville, R. S. 2002, MNRAS, 329, 246
Bundy, K., Ellis, R. S., Conselice, C. J., et al. 2006, ApJ, 651, 120
Bundy, K., Fukugita, M., Ellis, R. S., et al. 2009, ApJ, 697, 1369
Bundy, K., Scarlata, C., Carollo, C. M., et al. 2010, ApJ, 719, 1969
Busha, M. T., Wechsler, R. H., Behroozi, P. S., et al. 2010, arXiv:1011.6373
Cacciato, M., van den Bosch, F. C., More, S., et al. 2009, MNRAS, 394, 929
Capak, P., Aussel, H., Ajiki, M., et al. 2007, ApJS, 172, 99
Cattaneo, A., Dekel, A., Devriendt, J., Guiderdoni, B., & Blaizot, J. 2006, MNRAS, 370, 1651
Charlot, S., & Fall, S. M. 2000, ApJ, 539, 718
Collister, A. A., & Lahav, O. 2005, MNRAS, 361, 415
Conroy, C., Gunn, J. E., & White, M. 2009, ApJ, 699, 486
Conroy, C., Prada, F., Newman, J. A., et al. 2007, ApJ, 654, 153
Conroy, C., & Wechsler, R. H. 2009, ApJ, 696, 620
Conroy, C., Wechsler, R. H., & Kravtsov, A. V. 2006, ApJ, 647, 201
Cooray, A. 2006, MNRAS, 365, 842
Cowie, L. L., & Barger, A. J. 2008, ApJ, 686, 72
Cowie, L. L., Songaila, A., Hu, E. M., & Cohen, J. G. 1996, AJ, 112, 839

Crain, R. A., Theuns, T., Dalla Vecchia, C., et al. 2009, MNRAS, 399, 1773
Croton, D. J., Springel, V., White, S. D. M., et al. 2006, MNRAS, 365, 11
Davis, M., Faber, S. M., Newman, J., et al. 2003, Proc. SPIE, 4834, 161
Drory, N., Bender, R., Feulner, G., et al. 2004, ApJ, 608, 742
Drory, N., Bundy, K., Leauthaud, A., et al. 2009, ApJ, 707, 1595
Dunkley, J., Komatsu, E., Nolta, M. R., et al. 2009, ApJS, 180, 306
Dutton, A. A., Conroy, C., van den Bosch, F. C., Prada, F., & More, S. 2010, MNRAS, 407, 2
Efstathiou, G., Lake, G., & Negroponte, J. 1982, MNRAS, 199, 1069
Fakhouri, O., & Ma, C. 2010, MNRAS, 401, 2245
Fakhouri, O., Ma, C., & Boylan-Kolchin, M. 2010, MNRAS, 406, 2267
Feldmeier, J. J., Mihos, J. C., Morrison, H. L., et al. 2004, ApJ, 609, 617
Ferrarese, L., & Merritt, D. 2000, ApJ, 539, L9
Fontana, A., Salimbeni, S., Grazian, A., et al. 2006, A&A, 459, 745
Fontanot, F., De Lucia, G., Monaco, P., Somerville, R. S., & Santini, P. 2009, MNRAS, 397, 1776
Foucaud, S., Conselice, C. J., Hartley, W. G., et al. 2010, MNRAS, 406, 147
Gabor, J. M., Dave', R., Oppenheimer, B. D., & Finlator, K. 2011, MNRAS, 417, 2676
Gebhardt, K., Bender, R., Bower, G., et al. 2000, ApJ, 539, L13
Geha, M., Blanton, M. R., Masjedi, M., & West, A. A. 2006, ApJ, 653, 240
Gelman, A., & Rubin, D. 1992, Stat. Sci., 7, 457
George, M. R., et al. 2011, arXiv:1109.6040
Gilbank, D. G., Balogh, M. L., Glazebrook, K., et al. 2010, MNRAS, 405, 2419
Gilks, W. R., Richardson, S., & Spiegelhalter, D. J. 1996, in Markov Chain Monte Carlo in Practice (London: Chapman and Hall)
Gnedin, O. Y., Weinberg, D. H., Pizagno, J., Prada, F., & Rix, H. 2007, ApJ, 671, 1115
Gonzalez, A. H., Zabludoff, A. I., & Zaritsky, D. 2005, ApJ, 618, 195
Groth, E. J., & Peebles, P. J. E. 1977, ApJ, 217, 385
Guo, Q., White, S., Li, C., & Boylan-Kolchin, M. 2010, MNRAS, 404, 1111
Heymans, C., Bell, E. F., Rix, H.-W., et al. 2006a, MNRAS, 371, L60
Heymans, C., Van Waerbeke, L., Bacon, D., et al. 2006b, MNRAS, 368, 1323
Hinshaw, G., Weiland, J. L., Hill, R. S., et al. 2009, ApJS, 180, 225
Hoekstra, H. 2007, MNRAS, 379, 317
Hoekstra, H., Yee, H. K. C., & Gladders, M. D. 2004, ApJ, 606, 67
Hopkins, P. F., Bundy, K., Croton, D., et al. 2010a, ApJ, 715, 202
Hopkins, P. F., Murray, N., Quataert, E., & Thompson, T. A. 2010b, MNRAS, 401, L19
Ilbert, O., Capak, P., Salvato, M., et al. 2009, ApJ, 690, 1236
Johnston, D. E., Sheldon, E. S., Wechsler, R. H., et al. 2007, arXiv:0709.1159
Juneau, S., Glazebrook, K., Crampton, D., et al. 2005, ApJ, 619, L135
Kereš, D., Katz, N., Davé, R., Fardal, M., & Weinberg, D. H. 2009, MNRAS, 396, 2332
Kereš, D., Katz, N., Weinberg, D. H., & Davé, R. 2005, MNRAS, 363, 2
Koekemoer, A. M., Aussel, H., Calzetti, D., et al. 2007, ApJS, 172, 196
Koekemoer, A. M., Fruchter, A. S., Hook, R. N., & Hack, W. 2002, in The 2002 HST Calibration Workshop, ed. S. Arribas, A. Koekemoer, & B. Whitmore (Baltimore, MD: Space Telescope Science Institute), 337
Kravtsov, A. V., Berlind, A. A., Wechsler, R. H., et al. 2004, ApJ, 609, 35
Krick, J. E., Bernstein, R. A., & Pimbblet, K. A. 2006, AJ, 131, 168
Landy, S. D., & Szalay, A. S. 1993, ApJ, 412, 64
Leauthaud, A., Finoguenov, A., Kneib, J.-P., et al. 2010, ApJ, 709, 97
Leauthaud, A., George, M. R., Behroozi, P. S., et al. 2011a, arXiv:1109.0010
Leauthaud, A., Massey, R., Kneib, J.-P., et al. 2007, ApJS, 172, 219
Leauthaud, A., Tinker, J., Behroozi, P. S., Busha, M. T., & Wechsler, R. 2011b, ApJ, 738, 45
Lewis, A., & Bridle, S. 2002, Phys. Rev. D, 66, 103511
Li, C., & White, S. D. M. 2009, MNRAS, 398, 2177
Lilly, S. J., Le Fvre, O., Renzini, A., et al. 2007, ApJS, 172, 70
Mahdavi, A., Hoekstra, H., Babul, A., & Henry, J. P. 2008, MNRAS, 384, 1567
Mandelbaum, R., Seljak, U., Cool, R. J., et al. 2006a, MNRAS, 372, 758
Mandelbaum, R., Seljak, U., Kauffmann, G., Hirata, C. M., & Brinkmann, J. 2006b, MNRAS, 368, 715
Massey, R., Heymans, C., Bergé, J., et al. 2007, MNRAS, 376, 13
Massey, R., Stoughton, C., Leauthaud, A., et al. 2010, MNRAS, 401, 371
McBride, J., Fakhouri, O., & Ma, C. 2009, MNRAS, 398, 1858
McCracken, H. J., Capak, P., Salvato, M., et al. 2010, ApJ, 708, 202
McKay, T. A., Sheldon, E. S., Johnston, D., et al. 2002, ApJ, 571, L85
McKay, T. A., Sheldon, E. S., Racusin, J., et al. 2001, arXiv:astro-ph/0108013

Miralda-Escude, J. 1991, ApJ, 370, 1
Mo, H. J., Mao, S., & White, S. D. M. 1998, MNRAS, 295, 319
More, S., van den Bosch, F. C., Cacciato, M., et al. 2009, MNRAS, 392, 801
More, S., van den Bosch, F. C., Cacciato, M., et al. 2010, MNRAS, 410, 210
Moster, B. P., Somerville, R. S., Maulbetsch, C., et al. 2010, ApJ, 710, 903
Muñoz-Cuartas, J. C., Macciò, A. V., Gottlöber, S., & Dutton, A. A. 2011, MNRAS, 411, 584
Neistein, E., Li, C., Khochfar, S., et al. 2011, MNRAS, 416, 1486
Noeske, K. G., Weiner, B. J., Faber, S. M., et al. 2007, ApJ, 660, L43
Norberg, P., Frenk, C. S., & Cole, S. 2008, MNRAS, 383, 646
Panter, B., Jimenez, R., Heavens, A. F., & Charlot, S. 2007, MNRAS, 378, 1550
Parry, O. H., Eke, V. R., & Frenk, C. S. 2009, MNRAS, 396, 1972
Peacock, J. A., & Smith, R. E. 2000, MNRAS, 318, 1144
Pérez-González, P. G., Trujillo, I., Barro, G., et al. 2008, ApJ, 687, 50
Pizagno, J. L., II 2006, PhD thesis, Ohio State Univ.
Pizagno, J., Prada, F., Weinberg, D. H., et al. 2007, AJ, 134, 945
Prada, F., Vitvitska, M., Klypin, A., et al. 2003, ApJ, 598, 260
Rhodes, J. D., Massey, R. J., Albert, J., et al. 2007, ApJS, 172, 203
Rhodes, J., Refregier, A., & Groth, E. J. 2000, ApJ, 536, 79
Rix, H.-W., Barden, M., Beckwith, S. V. W., et al. 2004, ApJS, 152, 163
Sánchez, A. G., & Cole, S. 2008, MNRAS, 385, 830
Sargent, M. T., Carollo, C. M., Lilly, S. J., et al. 2007, ApJS, 172, 434
Schmidt, M. 1968, ApJ, 151, 393
Schrabback, T., Hartlap, J., Joachimi, B., et al. 2010, A&A, 516, A63
Scoccimarro, R., Sheth, R. K., Hui, L., & Jain, B. 2001, ApJ, 546, 20
Scoville, N., Aussel, H., Brusa, M., et al. 2007, ApJS, 172, 1
Seljak, U. 2000, MNRAS, 318, 203
Sheldon, E. S., Johnston, D. E., Frieman, J. A., et al. 2004, AJ, 127, 2544
Sheldon, E. S., Johnston, D. E., Scranton, R., et al. 2009, ApJ, 703, 2217
Shen, S., Mo, H. J., White, S. D. M., et al. 2003, MNRAS, 343, 978
Skibba, R. A., & Sheth, R. K. 2009, MNRAS, 392, 1080
Somerville, R. S., Hopkins, P. F., Cox, T. J., Robertson, B. E., & Hernquist, L. 2008, MNRAS, 391, 481
Springob, C. M., Haynes, M. P., Giovanelli, R., & Kent, B. R. 2005, ApJS, 160, 149
Tasitsiomi, A., Kravtsov, A. V., Wechsler, R. H., & Primack, J. R. 2004, ApJ, 614, 533
Tinker, J., Kravtsov, A. V., Klypin, A., et al. 2008, ApJ, 688, 709
Tinker, J. L., Norberg, P., Weinberg, D. H., & Warren, M. S. 2007, ApJ, 659, 877
Tinker, J. L., Wechsler, R. H., & Zheng, Z. 2010, ApJ, 709, 67
Vale, A., & Ostriker, J. P. 2004, MNRAS, 353, 189
Vale, A., & Ostriker, J. P. 2006, MNRAS, 371, 1173
Vale, A., & Ostriker, J. P. 2008, MNRAS, 383, 355
van den Bosch, F. C., Norberg, P., Mo, H. J., & Yang, X. 2004, MNRAS, 352, 1302
van den Bosch, F. C., Yang, X., & Mo, H. J. 2003, MNRAS, 340, 771
van den Bosch, F. C., Yang, X., Mo, H. J., et al. 2007, MNRAS, 376, 841
Wake, D. A., Whitaker, K. E., Labbé, I., et al. 2011, ApJ, 728, 46
Wechsler, R. H., Bullock, J. S., Primack, J. R., Kravtsov, A. V., & Dekel, A. 2002, ApJ, 568, 52
White, M., Blanton, M., Bolton, A., et al. 2011, ApJ, 728, 126
Wilson, G., Kaiser, N., Luppino, G. A., & Cowie, L. L. 2001, ApJ, 555, 572
Yang, X., Mo, H. J., & van den Bosch, F. C. 2003, MNRAS, 339, 1057
Yang, X., Mo, H. J., & van den Bosch, F. C. 2009, ApJ, 695, 900
Yoo, J., Tinker, J. L., Weinberg, D. H., et al. 2006, ApJ, 652, 26
Yoo, J., Weinberg, D. H., Tinker, J. L., Zheng, Z., & Warren, M. S. 2009, ApJ, 698, 967
Zehavi, I., Blanton, M. R., Frieman, J. A., et al. 2002, ApJ, 571, 172
Zehavi, I., Zheng, Z., Weinberg, D. H., et al. 2005, ApJ, 630, 1
Zehavi, I., Patiri, S., & Zheng, Z. 2011a, arXiv:1104.0389
Zehavi, I., Zheng, Z., Weinberg, D. H., et al. 2011b, ApJ, 736, 59
Zentner, A. R., Berlind, A. A., Bullock, J. S., Kravtsov, A. V., & Wechsler, R. H. 2005, ApJ, 624, 505
Zhang, J., & Komatsu, E. 2011, MNRAS, 414, 1047
Zheng, Z., Berlind, A. A., Weinberg, D. H., et al. 2005, ApJ, 633, 791
Zheng, Z., Coil, A. L., & Zehavi, I. 2007, ApJ, 667, 760
Zheng, Z., & Weinberg, D. H. 2007, ApJ, 659, 1
Zibetti, S., White, S. D. M., Schneider, D. P., & Brinkmann, J. 2005, MNRAS, 358, 949